STUDYING THE WARM HOT INTERGALACTIC MEDIUM WITH GAMMA-RAY BURSTS

E. Branchini[1], E. Ursino[1], A. Corsi[2], D. Martizzi[1], L. Amati[3], J. W. den Herder[4], M. Galeazzi[5], B. Gendre[6],
J. Kaastra[4,7], L. Moscardini[8,9], F. Nicastro[10], T. Ohashi[11], F. Paerels[4,12], L. Piro[2], M. Roncarelli[10,13], Y. Takei[4,14],
AND M. Viel[15,16]

[1] Dipartimento di Fisica, Università degli Studi "Roma Tre" via della Vasca Navale 84, I-00146 Roma, Italy; branchin@fis.uniroma3.it
[2] INAF-Istituto di Astrofisica Spaziale Fisica Cosmica, Via del Fosso del Cavaliere 100, I-00133 Roma, Italy
[3] INAF-Istituto di Astrofisica Spaziale e Fisica Cosmica Bologna, via P. Gobetti 101, I-40129 Bologna, Italy
[4] SRON Netherlands Institute for Space Research, Sorbonnelaan 2, 3584 CA Utrecht, The Netherlands
[5] Physics Department of University of Miami, 319 Knight Physics Building, Coral Gables, FL 33164, USA
[6] Laboratoire d'Astrophysique de Marseille/CNRS/Université de Provence, 38 Rue Joliot-Curie, 13388 Marseille CEDEX 13, France
[7] Astronomical Institute, University of Utrecht, Postbus 8000, 3508, TA Utrecht, Netherlands
[8] Dipartimento di Astronomia, Università degli Studi di Bologna, via Ranzani 1, I-40127 Bologna, Italy
[9] INFN/National Institute for Nuclear Physics, Sezione di Bologna, Via Berti Pichat 6/2, I-40127 Bologna, Italy
[10] INAF-Osservatorio Astronomico di Roma, via Frascati 33, I00040 Monteporzio-Catone (RM), Italy
[11] Department of Physics, School of Science, Tokyo Metropolitan University, 1-1 Minami-Osawa, Hachioji, Tokyo 192-0397, Japan
[12] Columbia Astrophysics Laboratory and Department of Astronomy, Columbia University, 550 West 120th Street, New York, NY 10027, USA
[13] Centre d'Étude Spatiale des Rayonnements (CESR) - CNRS, Observatoire Midi-Pyrénées, 9 avenue du Colonel Roche, 31028 Toulouse Cedex 04, France
[14] Institute of Space and Astronautical Science, Japan Aerospace Exploration Agency, 3-1-1 Yoshiodai, Sagamihara, Kanagawa 229-8510, Japan
[15] INAF-Osservatorio Astronomico di Trieste, via Tiepolo 11, I-34131 Trieste, Italy
[16] INFN/National Institute for Nuclear Physics, Via Valerio 2, I-34127 Trieste, Italy

ABSTRACT

We assess the possibility of detecting and characterizing the physical state of the missing baryons at low redshift by analyzing the X-ray absorption spectra of the gamma-ray burst (GRB) afterglows, measured by a microcalorimeter-based detector with 3 eV resolution and 1000 cm^2 effective area and capable of fast repointing, similar to that on board of the recently proposed X-ray satellites *EDGE* and *XENIA*. For this purpose we have analyzed mock absorption spectra extracted from different hydrodynamical simulations used to model the properties of the warm hot intergalactic medium (WHIM). These models predict the correct abundance of O VI absorption lines observed in UV and satisfy current X-ray constraints. According to these models space missions such as *EDGE* and XENIA should be able to detect ∼60 WHIM absorbers per year through the O VII line. About 45% of these have at least two more detectable lines in addition to O VII that can be used to determine the density and the temperature of the gas. Systematic errors in the estimates of the gas density and temperature can be corrected for in a robust, largely model-independent fashion. The analysis of the GRB absorption spectra collected in three years would also allow to measure the cosmic mass density of the WHIM with ∼15% accuracy, although this estimate depends on the WHIM model. Our results suggest that GRBs represent a valid, if not preferable, alternative to active galactic nuclei to study the WHIM in absorption. The analysis of the absorption spectra nicely complements the study of the WHIM in emission that the spectrometer proposed for *EDGE* and *XENIA* would be able to carry out thanks to its high sensitivity and large field of view.

Key words: cosmology: observations – gamma rays: bursts – intergalactic medium – large-scale structure of universe – line: identification

Online-only material: color figures

1. INTRODUCTION

According to the standard cosmological scenario, baryonic matter provides a small fraction, about 4%–5%, of the total cosmic energy content. While baryons are to first order dynamically negligible in shaping the large-scale structure of the universe, they have been the essential component in creating stars, galaxies, planets, and the life in the universe and constitute the only component that interacts with electromagnetic radiation. As such, they allow to study in great detail, through diverse observations, the physical conditions for the formation and evolution of cosmic structures.

As a matter of fact the baryon density in the Lyα forest at redshift 2–3 (Weinberg et al. 1997; Rauch 1998) accounts for a large fraction of the baryon mass as inferred from the predictions of the big bang nucleosynthesis combined with the measured abundances of the light elements (Burles & Tytler 1997, 1998)

and, independently, with the temperature fluctuations of the cosmic microwave background (CMB; Spergel et al. 2003; Komatsu et al. 2009). On the other hand, an observational census of cosmic baryons in the local universe (Fukugita et al. 1998; Fukugita & Peebles 2004; Danforth & Shull 2005) shows that at $z \sim 0$ only about 50% of the baryons have already been detected. The content of stars in galaxies and the interstellar medium (ISM) provides only about 8% of the overall baryonic budget; the hot plasma with temperature of at least 10^7 K contained in the potential wells of galaxy clusters adds an additional 11%. Finally, the diffuse gas with temperature below 10^7 K, which constitutes the local Lyα forest, provides a further 29% (Bregman 2007).

Hydrodynamical numerical simulations have provided a solution to this paradox within the framework of the "concordance" lambda cold dark matter (ΛCDM) model. They predict that about half of the total baryonic content of the universe at $z < 1$

should be in a warm hot phase with temperature in the range 10^5–10^7 K, distributed in a web of tenuous filaments (Cen & Ostriker 1999a). As such, the warm hot intergalactic medium (WHIM) represents the dominant component of baryons in the low-redshift universe. Its thermal evolution is primarily driven by shock heating from gravitational perturbations breaking onto unvirialized cosmic structures, such as large-scale filaments and virialized structures, such as galaxies, groups, and clusters of galaxies. Feedback effects related to the nuclear activity or to galactic superwinds from galaxy and star formation also play a role, especially in high-density environments (e.g., Cen & Ostriker 2006). These baryons are so hot and so highly ionized that they can only emit or absorb in the far UV and soft X-ray bands. However, the typical density of the WHIM being lower than that of the hot intracluster medium it is extremely hard to detect. Yet, it must contribute to the soft X-ray background. The importance of this contribution clearly depends on the physical conditions of the WHIM (e.g., Voit & Bryan 2001; Bryan & Voit 2001). The exquisite spatial resolution of the *Chandra* X-*Ray Observatory* has now allowed to resolve a large part, more than 80%, of the cosmic X-ray background at soft energies into the contribution of pointlike sources (mostly active galactic nuclei—AGNs hereafter). Hickox & Markevitch (2007a, 2007b) recently analyzed the Chandra Deep Fields North and South. After removing the contribution from X-ray, optical, and IR sources and carefully characterizing the instrumental background and noncosmological foreground, they computed the residual background. According to their analysis, this residual background in the 0.65–1 keV band cannot be accounted for by extrapolating the source number counts to lower fluxes. Instead, it comes interestingly close to the theoretical predictions of WHIM emission based on cosmological hydrodynamical simulations that include realistic description of star formation and SN feedback (e.g., Roncarelli et al. 2006). If due to soft X-ray emission from the diffuse gas, this residual X-ray background would represent the first, though indirect, detection of the missing baryons in emission.

Clearly, the study of the unresolved soft X-ray background just provides an upper limit to the amount of diffuse gas and indirect indications of its physical properties. The best chance to detect the WHIM is by observing the emission or absorption lines of highly ionized element such as C, N, O, Ne, and possibly Mg and Fe. The strongest lines expected correspond to the outer K (X-ray band) and L (far-UV band) shell transitions from H-like, He-like, and Li-like oxygen ions: the O VIII 1s–2p X-ray doublet (from now on simply O VIII), the O VII 1s–2p X-ray resonance line (O VII, hereafter), and the O VI UV doublet (O VI-UV). These measurements, however, are at the limit of current instrumentation's capability.

So far, the best WHIM detection has been provided by the analysis of the UV spectra of 31 AGNs by Danforth & Shull (2005). They detected 40 O VI-UV absorption systems counterparts to Lyα absorbers, whose cumulative number per unit redshift above a given equivalent width agrees with the latest theoretical predictions (Cen & Fang 2006). Most of the Lyα lines associated with these absorbers, however, are too narrow to be produced by gas at temperatures larger than 10^5 K. This means that either these lines are associated with the local Lyα forest, and thus their contribution to the total baryon budgets has been already accounted for (Tripp et al. 2008), or that two different gas phases are found at the same location: a photoionized gas responsible for the Lyα absorption and shock-heated WHIM responsible for the O VI lines. Assuming that all O VI-UV

lines are indeed produced by a multiphase gas, one obtains an upper limit to the mass density associated with these absorbers which corresponds to 7%–10% of the missing baryonic mass (Danforth & Shull 2005; Tripp et al. 2006). Alternatively, one could search for broad Lyα lines in the UV spectra, i.e., lines with a width parameter $b \geqslant 40$ km s^{-1} associated with gas hotter than 10^5 K. The recent searches by Richter et al. (2006) and Stocke et al. (2008) showed that the few broad absorbers detected so far contribute to 2%–10% of the mass of the missing baryons.

All these studies show that while some of the missing baryons have been revealed through O VI lines, the vast majority of them is too hot to produce significant O VI opacity. Therefore, the bulk of the WHIM can only be revealed and studied in the soft X-ray band. In emission, the diffuse signal detected in correspondence with overdensity of galaxies has been interpreted as the signature of the WHIM by Zappacosta et al. (2005) and by Mannucci et al. (2007). In absorption, among the several claimed WHIM detections at $z > 0$ (e.g., Fang et al. 2002; Mathur et al. 2003), the most convincing one has been provided by Nicastro et al. (2005) who detected several WHIM absorption lines in the X-ray spectrum of the extraordinarily bright blazar Mrk 421. Yet, the statistical significance of these detections has been questioned by Kaastra et al. (2006) through Monte Carlo simulations. Moreover, the absorption lines originally seen in the spectrum obtained with the Low-Energy Transmission Grating Spectrometer on board *Chandra* were not detected in a spectrum of the same object subsequently obtained through a longer exposure with the Reflection Grating Spectrometer on *XMM-Newton* (Rasmussen et al. 2007). The very existence of this unsettled controversy demonstrates the importance of performing a dedicated experiment to detect the missing baryons in the X-ray band. Even more, going beyond the mere detection of the WHIM, the characterization of its thermal and chemical properties, will open an unexplored territory for the study of the interaction and coevolution of the diffuse phase of cosmic baryons and the stellar population.

The possibility of detecting the WHIM in the absorption spectra of X-ray bright objects like AGNs has been thoroughly discussed from a theoretical perspective in a series of studies. While Chen et al. (2003) and Cen & Fang (2006), to mention a few examples, addressed the problem in a generic cosmological setup, other authors (e.g., Kravtsov et al. 2002; Klypin et al. 2003; Viel et al. 2005) focused on the gas distribution in the local universe. In addition, other works have specialized the treatment to some specific satellites, such as *XMM-Newton* (Kawahara et al. 2006) or the proposed *DIOS* (Yoshikawa et al. 2003; Yoshikawa et al. 2004), *XEUS*, and *Constellation-X* (Viel et al. 2003) satellites. A comprehensive review of the current and future instrumentation for the study of the WHIM can be found in Paerels et al. (2008). In this work, we focus on the possibility of revealing the missing baryons signature in the X-ray spectra of the GRB afterglows. The idea of using GRBs as bright X-ray beacons to study the physical properties of the intervening gas and trace its evolution out to very large redshifts has been first proposed by Fiore et al. (2000). Here, we push this idea further and exploit the recent *Swift* results on the rate of bright GRBs to estimate the probability to detect the WHIM and to characterize its physical status in the context of the recently proposed *EDGE* and *XENIA* space missions. In addition, rather than relying on some specific theoretical prediction, we consider different WHIM models obtained from hydrodynamical simulations to account for theoretical uncertainties.

The characteristics of the detectors on board of *EDGE* and *XENIA* can be found in Piro et al. (2009), Kouveliotou et al. (2008), and at the Web site http://projects.iasf-roma.inaf.it/EDGE. GRBs are localized by a Wide-Field Monitor (WFM), a hard X-ray detector covering about 1/4 of the sky. The position derived on board is used to command a satellite autonomous slew, which enables the acquisition of the GRB location by the Wide-Field Spectrometer (WFS), an X-ray telescope equipped with high spectral resolution TES microcalorimeters, in 60 s.

Here, we list for reference the capabilities of the two instruments that are more relevant to this work.

1. WFS: energy range $0.2 - 2.2$ keV. Energy resolution $\Delta E = 3$ eV (goal: 1 eV) at 0.5 keV (TES microcalorimeters). Field of view (FOV) $0°7 \times 0°7$. Effective area $A = 1000$ cm^2 at 0.5 keV. Angular resolution: $\Delta\theta = 2$ arcmin.
2. WFM: energy range $6 - 200$ keV. Energy resolution $\Delta E/E = 3\%$ at 100 keV. $FOV > 2.5$ sr. Effective area $A = 1000$ cm^2 at 100 keV. Location accuracy: $\Delta\theta = 3$ arcmin.

This work is organized as follows. In Section 2, we describe our WHIM models and discuss the characteristics of the hydrodynamical simulations that we have used to extract the mock X-ray absorption spectra. In Section 3, we analyze the statistical properties of the absorption lines in the mock X-ray spectra, characterize the physical properties of the absorbing material, and investigate the statistical correlations among the absorption lines. In Section 4, we quantify the probability of detecting WHIM lines in the GRB afterglow spectra and estimate the number of detections expected with a satellite such as *XENIA* or *EDGE*. In Section 5, we investigate the possibility of studying the physical status of the WHIM and measuring its cosmological abundance. We discuss our main results and conclude in Section 6.

2. MODELING THE WHIM

The best WHIM models currently available are based on numerical hydrodynamical simulations and provide robust predictions for the cosmological WHIM abundance as a function of redshift, the filamentary appearance of its large-scale distribution, and its thermal state (Cen & Ostriker 1999a, 1999b, 2006; Chen et al. 2003 to provide a few examples). The latter is mainly determined by hydrodynamical shocks resulting from the buildup of cosmic structures at scales that have become nonlinear. Additional, nongravitational heating mechanisms that depend on the little known feedback processes following star formation in galaxies. However, they are relevant only in high-density environments in which the role of radiative cooling must also be taken into account. In this work, we do not rely on a single WHIM model that includes sophisticated recipes to treat feedback effects. Instead, in an attempt to bracket model uncertainties, we use two different hydrodynamical simulations to develop three WHIM models with different phenomenological treatments of the nongravitational heating mechanisms, star formation, and feedback effects.

The first WHIM model (dubbed model *M* in Table 1) relies on the same simulations described in Pierleoni et al. (2008). This numerical experiment, of which we only consider the outputs at $z \leqslant 1$, was performed with the GADGET-2 Lagrangian code (Springel 2005) in a computational box of size $60\,h^{-1}$ comoving Mpc, loaded with 480^3 dark matter (DM) and 480^3 gas particles. The Plummer equivalent gravitational softening was set equal to 2.5 kpc h^{-1} in comoving units for all particles. This
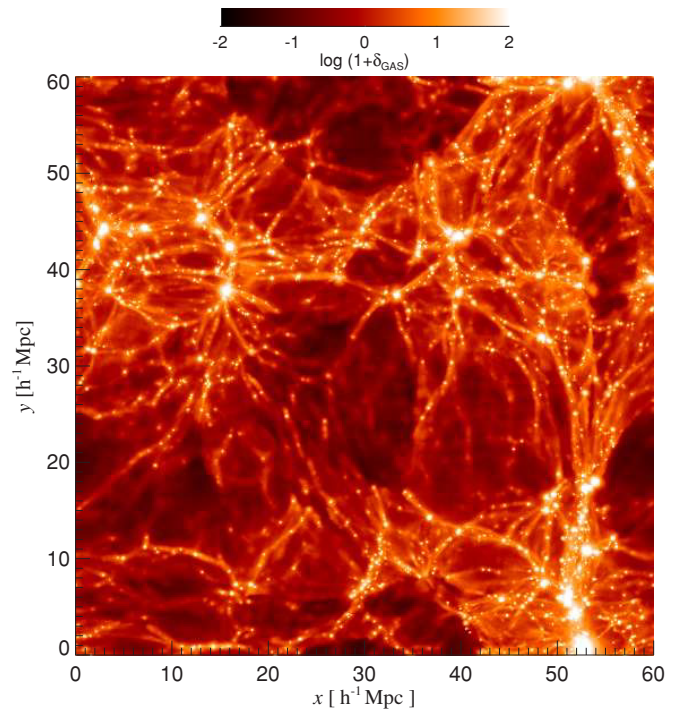

Figure 1. Spatial distribution of the gas overdensity δ_g in a slice of thickness 6 Mpc h^{-1} (comoving) at $z = 0$ extracted from the simulations described in Pierleoni et al. (2008) and centered around the largest cluster in the simulation box (to be found in the bottom-right part of the panel).

(A color version of this figure is available in the online journal.)

choice of parameters represents a good compromise between box size and resolution and allows to investigate the WHIM properties down to the Jeans scale. Radiative cooling and heating processes were followed according to Katz et al. (1996). The simulation assumes the same X-ray and UV background at $z = 0$ that Viel et al. (2003, 2004) used to determine the ionization state of the intergalactic gas. The X-ray background is not computed self-consistently but is modeled a posteriori as $I_X = I_X^0 (E/E_X)^{-1.29} \exp(-E/E_X)$, with $I_X^0 = 1.75 \times 10^{-26}$ erg cm^{-2} Hz^{-1} sr^{-1} s^{-1} and $E_X = 40$ keV, in agreement with observations (Boldt 1987; Fabian & Barcons 1992; Hellsten et al. 1998). The UV background is of the form $I_{UV} = I_{UV}^0 (E/13.6 \text{ eV})^{-1.8}$, with $I_{UV}^0 = 2.3 \times 10^{-23}$ erg cm^{-2} Hz^{-1} sr^{-1} s^{-1}, which agrees within a factor of 2 with the estimate of Shull et al. (1999) and shows no appreciable differences with the intrinsic Haardt–Madau like spectrum (Haardt & Madau 1996) used in the simulation run. The cosmological parameters of this simulation are similar to the *WMAP*-one year values (Spergel et al. 2003) and refer to a flat ΛCDM "concordance" model with $\Omega_\Lambda = 0.3$, $\Omega_b = 0.0463$, $H_0 = 72$ km s^{-1} Mpc^{-1}, $n = 0.95$, and $\sigma_8 = 0.85$. In Figure 1, we show the gas distribution at $z = 0$ of a slice of thickness 6 Mpc h^{-1} (comoving) extracted from the computational box.

The star formation criterion simply converts all gas particles whose temperature falls below 10^5 K and whose density contrast is larger than 1000 into (collisionless) star particles. No energy feedback from supernova explosions, metal ejection, and diffusion was considered. After determining the thermal state of each gas particle we assign the metal abundance in the postprocessing phase according to a phenomenological metallicity–density relation, calibrated on hydrodynamical simulations in which metal enrichment is treated self-consistently. In model *M*, we have assumed the deterministic relation $Z = \min(0.2, 0.02(1 + \delta_g)^{1/3})$ of Aguirre et al. (2001), where Z is the gas metallicity in solar

Table 1
WHIM Models

Model	$L_{\rm Box}$	$N_{\rm DM} + N_{\rm gas}$	ϵ	Ω_b	σ_8	Z–$\rho_{\rm g}$ Relation
M	60	$400^3 + 400^3$	2.5	0.046	0.85	$Z \propto \rho_{\rm g}^{1/3}$
$B1$	192	$480^3 + 480^3$	7.5	0.04	0.8	$Z\;Z \propto \rho_{\rm g}^{1/2}$
$B2$	192	$480^3 + 480^3$	7.5	0.04	0.8	Z–$\rho_{\rm g}$ + scatter

Notes. Column 1: model name; Column 2: box size (in comoving Mpc h^{-1}); Column 3: number of DM and gas particles; Column 4: Plummer equivalent gravitational softening (in kpc h^{-1}); Column 5: baryon density parameter; Column 6: mass variance at 8 Mpc h^{-1}; Column 7: metallicity–density relation adopted.

Table 2
Simulated WHIM Ions

Ion	Energy (eV)	f
O VI	11.95+12.01	0.19
O VI $1s$–$2p$	563	0.53
O VII $1s$–$2p$	574	0.70
O VII $1s$–$3p$	666	0.15
O VIII $1s$–$2p$	654	0.42
C V $1s$–$2p$	308	0.65
C VI $1s$–$2p$	367	0.42
Ne IX $1s$–$2p$	922	0.72
Fe XVII $2p$–$3d$	826	3.00
Mg XI $1s$–$2p$	1352	0.74

Notes. Column 1: ion; Column 2: wavelength (eV); Column 3: oscillator strength.

units and $\delta_{\rm g} \equiv \rho_{\rm g}/\langle\rho_{\rm g}\rangle - 1$ is the gas overdensity with respect to the mean, $\langle\rho_{\rm g}\rangle$. To model the WHIM properties we have used all available outputs of the hydrosimulation with $z \leqslant 1$ using the stacking technique described in Roncarelli et al. (2006).

The second simulation that we use has been carried out by Borgani et al. (2004) using the same GADGET-2 code. The box size is larger that in the previous case and consists of a comoving cube of 192 Mpc h^{-1} side containing 480^3+480^3 dark matter and gas particles. The Plummer-equivalent gravitational softening is $\epsilon = 7.5h^{-1}$ kpc at $z = 0$, fixed in physical units between $z = 2$ and $z = 0$ and fixed in comoving units at earlier times. The cosmological model is a flat ΛCDM with $\Omega_\Lambda = 0.7$, $\Omega_{\rm b} = 0.04$, $H_0 = 70$ km s^{-1} Mpc^{-1}, and $\sigma_8 = 0.8$. Differently from the previous case, this simulation includes a treatment of the main nongravitational physical processes that influence the physics of the gas: (1) the star formation mechanism that is treated adopting a subresolution multiphase model for the ISM (Springel & Hernquist 2003), (2) the feedback from SNe including the effect of weak galactic outflows, and (3) the radiative cooling assuming zero metallicity and heating/cooling from the uniform, time-dependent, photoionizing UV background by Haardt & Madau (1996).

We have used all available outputs of the simulation with $z \leqslant 1$ to construct two more WHIM models that differ by their metallicity–density relation. The rational behind specifying the metal abundance in the postprocessing phase rather than adopting the one computed self-consistently in the simulation is that the simple metal diffusion mechanism in the SPH code reproduces the correct metallicity in high-density regions like the intracluster medium, but underestimates the metal abundance in low-density environments like the WHIM. The first model obtained from the simulation of Borgani et al. (2004), dubbed $B1$ in Table 1, assumes the deterministic metallicity–density relation of Croft et al. (2001): $Z = \min(0.3, 0.005(1 + \delta_{\rm g})^{1/2})$. Several hydrodynamical experiments (e.g., Cen & Ostriker 1999a, 2006) have revealed that the relation between Z and $\delta_{\rm g}$ is characterized by a very large, non-Gaussian scatter around the mean, reflecting the fact that the thermal state and the metal content of the gas are not uniquely determined by the local density but, rather, by its dynamical, chemical, and thermal history. In model $B2$, we account for this stochasticity by enforcing in our hydrodynamical simulation the same scatter found by Cen & Ostriker (1999a, 1999b) in their numerical experiment. To do this we have measured the density–metallicity relation in the simulation outputs of Cen & Ostriker (1999a) and constructed a two-dimensional probability distribution in the Z–$\delta_{\rm g}$ plane by counting particles in each bin, at various redshifts. The resulting two-dimensional grid provides a probability distribution that we implement in a Monte Carlo procedure to assign metallicity to the gas particles in the Borgani et al. (2004) simulation with known density.

The rationale behind considering three different WHIM models is to provide some indication of the theoretical uncertainties that reflect our little understanding of the effects of stellar feedback from star and galaxy formation, chief among which is of course the metal enrichment. The latter is so important in determining the observational properties of the WHIM that model predictions obtained by specifying gas metallicity in the postprocessing phase come close to those computed self-consistently in the simulations (Chen et al. 2003). In what follows we mainly focus on model $B2$ that we regard as more realistic. However, we also consider the two models $B1$ and M, which adopt ideal metallicity models directly used in previous analyses that have appeared in the literature. We stress that these models do not bracket all unknowns in the theoretical calculation since they adopt simple recipes for metal enrichment and stellar feedback processes and ignore departure from local equilibrium that, instead, have been considered in the more sophisticated WHIM model of Cen & Fang (2006)

After having simulated the metals and their distribution in the box and after having specified the metagalactic UV and X-ray background, we have used the photoionization code CLOUDY (Ferland et al. 1998) to compute the ionization states of these metals under the hypothesis of hybrid collisional and photoionization equilibrium. The resulting ionization fractions turns out to be very similar to that obtained by Chen et al. (2003) and shown in their Figures 2 and 3 that implies that our O VII fraction in regions of moderate overdensity is different from that computed by Kawahara et al. (2006) using a modified SPEX code (see their Figure 1). The density of each ion was obtained through: $n_I(x) = n_H(x)X_I Y_{Z_\odot} Z$, where X_I is the ion fraction determined by CLOUDY that depends on gas temperature, gas density, and ionizing background, n_H is the density of hydrogen atoms, Z is the metallicity of the element in solar units, and $Y_{Z_\odot}$ is the solar abundance of the element (Asplund et al. 2005).

The ions responsible for the most prominent X-ray absorption lines are listed in Table 2 together with the energy of the transition and the oscillator strength. These are the X-ray lines that we simulate in our mock absorption spectra. In addition, to compare model predictions with existing data we also consider the O VI UV doublet (at 11.95 eV, 12.01 eV), which has been observed in the absorption spectra taken by *Far Ultraviolet Spectroscopic Explorer* (*FUSE*) and *Hubble Space Telescope* (*HST*; Tripp et al. 2000; Savage et al. 2002; Danforth & Shull 2005).

To check the validity of the hybrid ionization-collisional equilibrium hypothesis, we have computed the typical
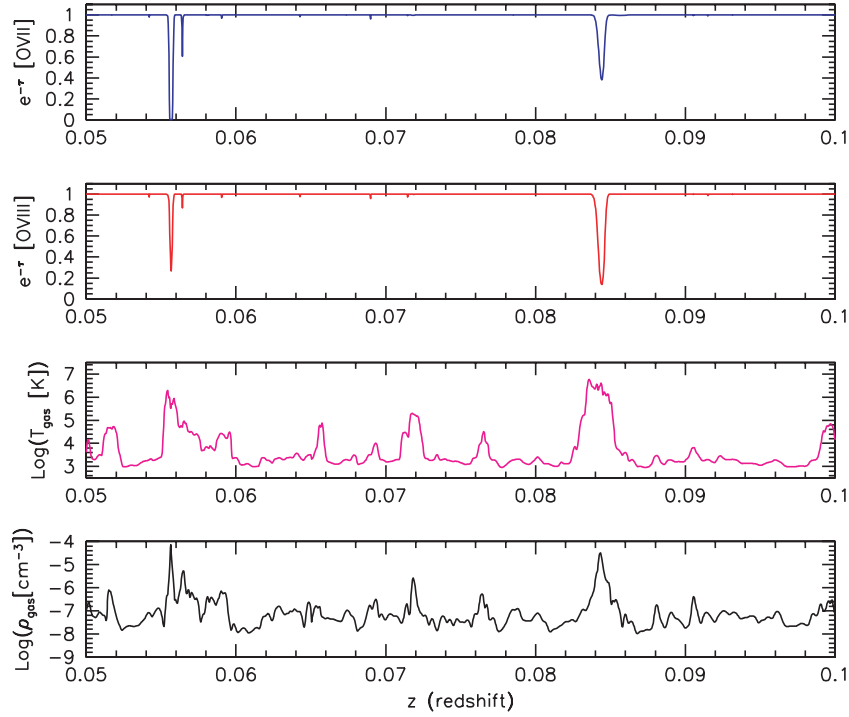
Figure 2. Simulated spectrum from model $B1$ for a generic LOS with two strong absorbers. From top to bottom: transmitted flux for O VII, O VIII, temperature, and density along the LOS as a function of redshift.

(A color version of this figure is available in the online journal.)

recombination time in the WHIM $t_{rec} = (n_{WHIM}\,\alpha_{rec})^{-1}$, with α_{rec} being the recombination rate. For the two more relevant ions, O VII and O VIII, in the temperature ranges considered here we find $\alpha_{rec} \sim 2 \times 10^{-11}$ cm^3 s^{-1} (Mazzotta et al. 1998), where both the dielectronic and radiative recombinations are taken into account. This means that the Hubble time is larger than the recombination time for a density $\geqslant 10^{-7}$ cm^{-3}. Thus, for a large fraction of the WHIM, the approximation of photoionization equilibrium should be reasonable. Indeed, as it has been shown by Yoshikawa & Sasaki (2006), departures from equilibrium do not dramatically alter the equivalent widths (EW hereafter) of the O VIII and O VII absorption lines.

2.1. Mock Absorption Spectra

Having determined the density of a given ion along the line of sight (LOS), the optical depth in redshift-space at velocity u (in km s^{-1}) is

$$\tau_I(u) = \frac{\sigma_{0,I}c}{H(z)} \int_{-\infty}^{\infty} dy\, n_I(y) \mathcal{V}\left[u - y - v_{\parallel}^I(y), b(y)\right], \quad (1)$$

where $\sigma_{0,I}$ is the cross section for the resonant absorption which depends on the wavelength, λ_I and the oscillator strength f_I of the transition, y is the real-space coordinate (in km s^{-1}), $\mathcal{V}$ is the standard Voigt profile normalized in real space, $b = (2k_B T/m_I c^2)^{1/2}$ is the thermal width. Ignoring the effect of peculiar velocities, i.e., setting $v_{\parallel}^I = 0$, the real-space coordinate y and the redshift z are related through $d\lambda/\lambda = dy/c$, where $\lambda = \lambda_I(1+z)$. Since WHIM absorbers have low column densities, the Voigt profile is well approximated by a Gaussian: $\mathcal{V} = (\sqrt{\pi} b)^{-1} \exp(-(u-y)^2/b^2)$. The transmitted flux is simply $\mathcal{F} = \exp(-\tau)$.

For each WHIM model we have extracted 15 independent spectra from the light cones obtained by stacking all available
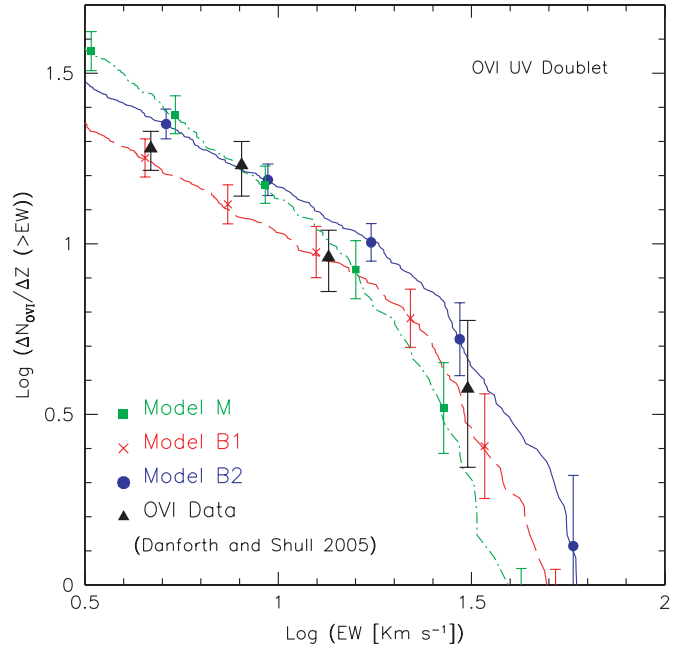

Figure 3. Cumulative distribution function of O VI UV doublet equivalent widths. Model predictions vs. observations. Filled triangles with error bars: Danforth & Shull (2005) measurements. Filled squares and dot-dashed green line: model M. Crosses and dashed red line: Model $B1$. Filled dots and solid blue line: Model $B2$. For each model the error bars represent the scatter in the 15 independent mock spectra.

(A color version of this figure is available in the online journal.)

simulation outputs. Mock spectra from model M have a spectral resolution of 3 km s^{-1} and extend out to $z = 0.5$. Spectra from models $B1$ and $B2$ have a resolution of ~ 9 km s^{-1} and extend out to $z = 1.0$. Figure 2 shows, for model $B1$, and from top

to bottom, the transmitted flux in O VII, O VIII, the density and the temperature along a generic LOS, out to $z = 0.1$. Strong absorption features are found in correspondence of density and temperature peaks. O VIII lines sample regions of higher density and temperature than O VII lines. The typical number of absorbers is small and they can be easily identified in the mock spectra using a simple threshold algorithm. The positions of the absorption lines are identified with the minima of the transmitted flux and their EW are measured by integrating $\mathcal{F}(u)$ over the redshift interval $[\underline{z}, \overline{z}]$ centered around the minimum, in which $\mathcal{F} \leqslant \mathcal{F}_{thr}$. The few overlapping lines are separated in correspondence of the local maximum between the two minima. The threshold to identify absorption lines is $\mathcal{F}_{thr} = 0.95$. We have checked that results do not change significantly if one lowers the threshold to 75% of the transmitted flux.

3. LINE STATISTICS

To check the reliability of our WHIM models we first compare our theoretical predictions with the only WHIM unambiguous detections available so far. In Figure 3, the different symbols connected by continuous lines show the cumulative distributions of O VI UV doublet EW$_s$ predicted by our models. Error bars represent the scatter among the different mock spectra. Filled triangles with error bars show the cumulative EW distribution of the O VI absorbers measured by Danforth & Shull (2005). Over most of the EW range, all of the considered WHIM models are consistent with data within the errors. The spread in model predictions reflects theoretical uncertainties. The larger number of O VI lines in model $B2$ results from the scatter in the density–metallicity relation that systematically increases the probability of an O VI absorption line. Model M predicts a cumulative distribution steeper than models $B1$ and $B2$. At large EW$_s$ the discrepancy reflects the different amount of large-scale power in the computational boxes of the parent simulations. At small EW$_s$, instead, the difference originates from the different numerical resolution of the two simulations. In this work, we focus on absorption lines with EW $\geqslant 10$ km s^{-1}. Hereafter, we use different units for the line EW$_s$. Useful conversions between units are EW $= 6.67(EW/100$ km s$^{-1})(\lambda/20$ Å) mÅ $= 0.33(EW/100$ km s$^{-1})(E/1$ keV) eV.

The scatter in the model predictions for the O VI line distribution function is quite small and one may wonder whether this is also the case for the X-ray absorption lines. Let us consider the two strongest WHIM lines: O VII and O VIII. These ions probe regions of higher density and temperature than O VI. In such environments the predicted ion abundance is more sensitive to the different metallicity–density prescriptions adopted in the models and thus we expect a larger spread among model predictions. Figure 4 shows that this is indeed the case: the differences among the predicted cumulative distributions for O VII (left panel) and O VIII (right panel) are larger than in the O VI case. Predictions of model $B2$, which account for the scatter in the metallicity, are consistent with those of the Chen et al. (2003) model, in which the metallicity is drawn randomly from a lognormal distribution with $\langle Z/Z_\odot \rangle = -1.0$, $\sigma_{\log Z} = 0.4$. Model $B2$ predictions are also consistent with those of Cen & Fang (2006) that include the feedback effect of galactic superwinds and account for departures from local thermodynamic equilibrium. We note that all our predictions, including those from models M and $B1$, satisfy the current upper limits on the O VII and O VIII line observations.

In Figure 5, we show, for model $B2$ only, the predicted cumulative distribution functions for the other ions listed in
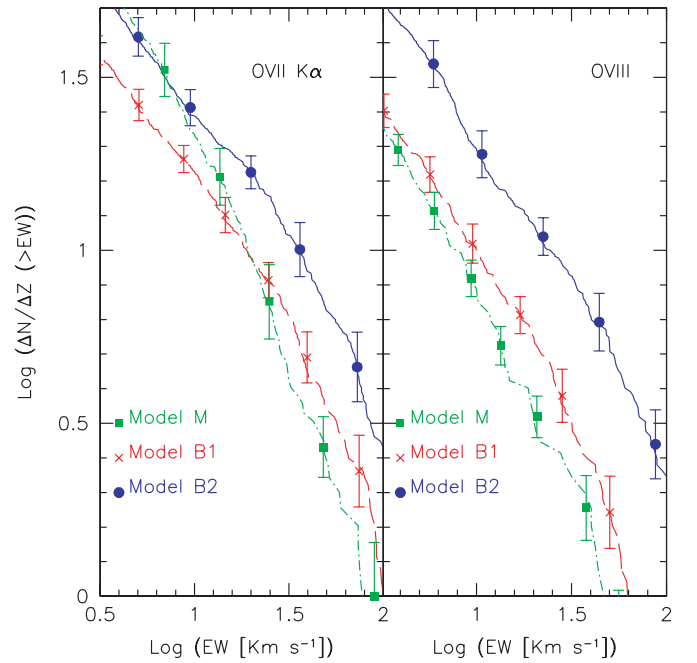

Figure 4. Cumulative distribution function of absorption lines EW$_s$. Model predictions. Left: cumulative distribution function of O VII. Right: cumulative distribution function of O VIII. Filled squares and dot-dashed green line: model M. Crosses and dashed red line: model $B1$. Filled dots and solid black line: model $B2$. Error bars in the model represent the scatter among the 15 independent mock spectra.

(A color version of this figure is available in the online journal.)

Table 2. As already pointed out by Chen et al. (2003) C VI and C V are the strongest absorption lines after oxygen. However, their transition energies of 367 and 308 eV put them in a range of poor instrument sensitivity (see Figure 10 below) and restrict their observability to low-redshift sources. Ne IX produces the next strongest absorption together with the O VII 1s–3p line. The latter, however, is observed in association with the stronger O VII 1s–2p line and, as we will discuss in the next section, improves the statistical significance of the WHIM detection, but offers no further information on the absorber's physical state. On the contrary, the O VI line in the X-ray band could, together with O VII and O VIII, be used to determine unambiguously the physics of the gas. Unfortunately the X-ray O VI line is typically $\sim$4 times weaker than the O VII line and will be difficult to detect unless instrumental sensitivity will increase dramatically. For this ion UV spectroscopy appears as the only effective option currently available.

3.1. Physical Properties of Mock Absorbers

Thanks to our WHIM models we can substantiate our previous statement that observed O VI lines have probed a few percent of the missing baryons that reside in the relatively cool regions. In Figure 6, we show the phase-space diagram of the cosmic baryons at $z \sim 0$ in the hydrodynamical simulation of Borgani et al. (2004). Small-size points represent gas particles in the simulation. Some regions of this phase-space diagram have been already probed by observations, like the X-ray emitting gas in the central regions of virialized objects (the green points with $T_g \gtrsim 10^{6.5}$ K and $\rho_g/\langle \rho_g \rangle \gtrsim 10^{2.5}$), the diffuse, cold gas responsible for the local Lyα forest (blue points with $T_g \leqslant 10^5$ K and $\rho_g/\langle \rho_g \rangle \leqslant 10^3$) and the cold, dense gas observed in association with star-forming regions within galaxies (yellow points
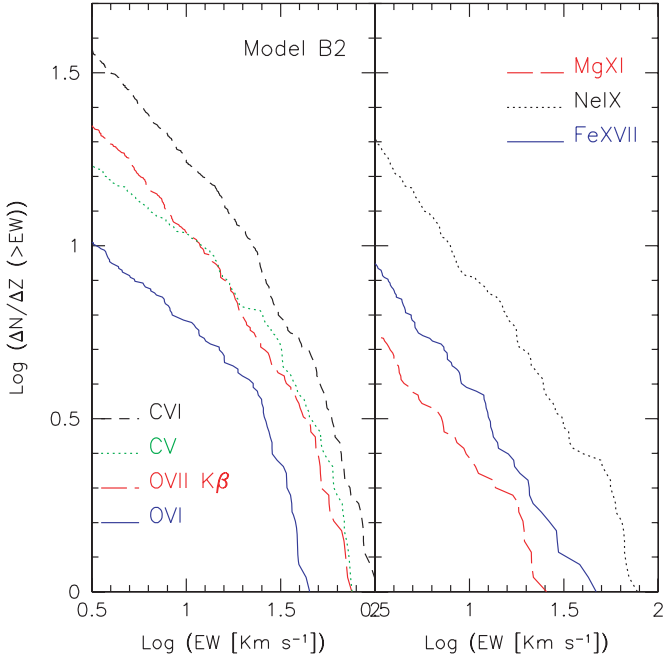
Figure 5. Cumulative distribution function of absorption lines equivalent widths. Predictions of model *B*2. Left: cumulative distribution function of O vi X-ray (blue continuous) O vii 1s–3p (red long-dashed), C v (green dotted), and C vi (black short-dashed). Right: cumulative distribution function of Fe xvii (blue solid), Mg xi (red long-dashed), and Ne ix (black dotted).

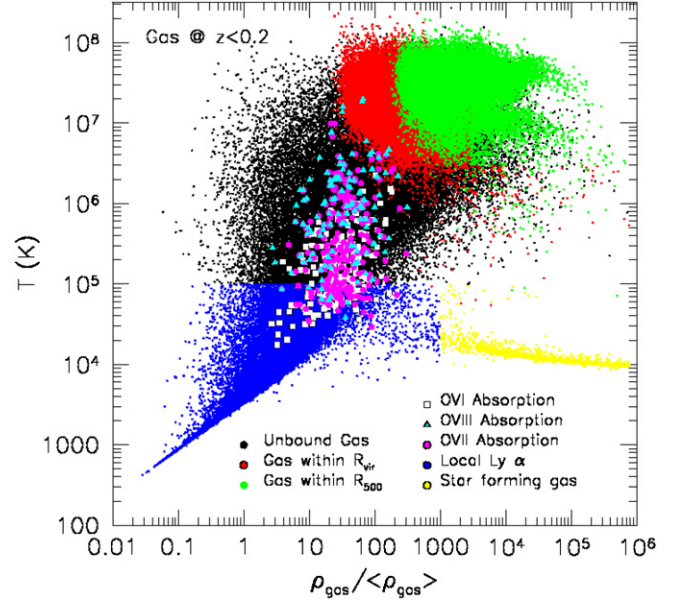(A color version of this figure is available in the online journal.)

Figure 6. Phase space diagram of the cosmic baryons at $z < 0.2$ from the hydrodynamical simulation of Borgani et al. (2004). Blue dots with $T \leqslant 10^5$ and $\rho/\langle\rho\rangle \leqslant 10^3$: gas particles detected in the local Ly α forest. Yellow dots with $T_g \leqslant 10^5$ K and $\rho_g/\langle\rho_g\rangle \geqslant 10^3$ gas particles associated with star forming regions. Green dots with $T_g \gtrsim 10^{6.5}$ and $\rho_g/\langle\rho_g\rangle \gtrsim 10^{2.5}$ gas particles in the central part of virialized structures that are potentially observable with current X-ray satellites. Red dots with $T_g \lesssim 10^{6.5}$ and $10^{1.5} \lesssim \rho_g/\langle\rho_g\rangle \lesssim 10^{2.5}$ gas particles in the outskirts of virialized objects currently not observed. Black dots: currently unobserved intergalactic medium including the warm hot phase. Filled white squares gas detectable through O vi absorption lines. Filled magenta dots gas detectable through O vii absorption lines. Filled cyan triangles gas detectable through O viii absorption lines. Only absorption lines with EW $\geqslant$ 10 km s^{-1} have been considered.

(A color version of this figure is available in the online journal.)

with $T_g \leqslant 10^5$ K and $\rho_g/\langle\rho_g\rangle \geqslant 10^3$). The majority of the remaining baryons are located in regions of the phase space that are currently not probed by observations. Some of them are expected to be found in the outskirts of the galaxy clusters all the way out to the virial radius (red points with $T_g \lesssim 10^{6.5}$ K and $10^{1.5} \lesssim \rho_g/\langle\rho_g\rangle \lesssim 10^{2.5}$) but the large majority, which constitute the bulk of the WHIM, is to be found in lower density environments.

The larger symbols characterize the gas that can be detected through O vi (filled white squares), O vii (filled magenta dots), or O viii (filled cyan triangles) assuming model *B*2. Only lines with EW $\geqslant$ 10 km s^{-1} are considered in the plot. Different ions preferentially probe different regions of the phase space with a non-negligible overlap, spanning a large range of WHIM physical conditions. As anticipated, O vi is a signpost for the cooler regions of the WHIM while, on the opposite, the O viii lines typically flag hotter environments. The O vii absorbers span a very large range in temperature, although those with $T_g < 10^5$ K are typically associated with weak lines.

The position of the O vi, O vii, and O viii symbols in the phase space is not determined precisely since the density and the temperature of the gas associated with the absorption line are not uniquely defined. In this work, we estimate temperature and density of the absorbing material as in Chen et al. (2003). First we define the temperature and density in each spectral bin as

$$\rho_g(u) = \frac{1}{\tau(u)} \int \frac{d\tau}{dy} \rho_g(y) dy; \quad T_g(u) = \frac{1}{\tau(u)} \int \frac{d\tau}{dy} T_g(y) dy \tag{2}$$

and then we obtain the corresponding quantities for the absorbers by averaging over the bins in the line redshift interval $[\underline{z}, \overline{z}]$. This is the definition that we have used to plot the symbols in Figure 6.

We have also considered an alternative estimator in which temperature and density are weighted by the optical depth of the line:

$$\hat{\rho}_g = \frac{\int_{\underline{z}}^{\overline{z}} \tau(y)\rho_g(y) dy}{\int_{\underline{z}}^{\overline{z}} \tau(y) dy}; \qquad \hat{T}_g = \frac{\int_{\underline{z}}^{\overline{z}} \tau(y)T_g(y) dy}{\int_{\underline{z}}^{\overline{z}} \tau(y) dy}. \tag{3}$$

Using Equation (3) rather Equation (2) does not introduce systematic differences, just a random scatter of ∼15% in both temperature and density.

Another possible source of ambiguity in estimating the temperature and the density of the gas is represented by those absorption systems characterized by two or more ions, each one with its own opacity. In this case, the redshift interval $[\underline{z}, \overline{z}]$ depends on the ion considered and so will be the estimated temperature and density of the absorbing gas. To assess the importance of this effect we have considered all mock absorption systems featuring any two lines among O vi, O vii, or O viii and found ∼20% scatter in temperature and density computed in the redshift ranges of the different lines.

3.2. Correlation between Absorbers

Figure 7 shows the predicted correlation between the equivalent widths of the oxygen lines associated with the same absorber in the mock spectra of model *B*2. We only consider absorbers in which all lines are detected above threshold. To avoid ambiguity we measure the line EW in the velocity range used to identify the O vii line. In the plots, the crosses indicate lines that are not saturated (i.e., for which the transmitted flux is above zero).
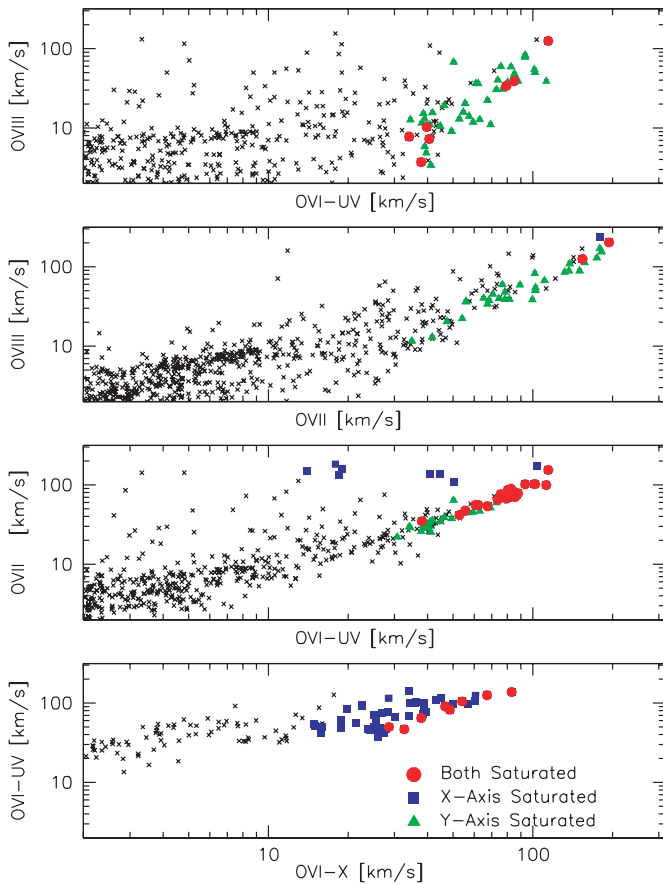
Figure 7. Equivalent width correlation for oxygen ions. From top to bottom: O VIII vs. O VI-UV, O VIII vs. O VII, O VII vs. O VI-UV, O VI-UV vs. O VI-X. The black crosses indicate unsaturated lines. Filled green triangles: saturated line for the absorber on the X-axis. Filled blue squares: saturated line for the absorber on the Y-axis. Filled red circles: both ion lines saturated.

(A color version of this figure is available in the online journal.)

The green triangles (blue squares) indicate absorbers in which the ion line on the X (Y) axis is saturated. The red dots indicate that both ion lines are saturated. The bottom panel shows the correlation between the equivalent widths of the O VI UV-doublet and the O VI X-ray line. For optically thin lines there is a simple, deterministic relation between the EW_s of the two lines. The scatter in the plot arises from having measured the EW of the lines in the velocity range appropriate for the O VII line. Equivalent widths of saturated UV-absorbers deviate from the expected correlation, causing the flattening at large EW_s. There is a small range of temperatures in which both O VII and O VI have high fractional abundance. In this interval both species trace the underlying baryon density, causing the tight correlation seen in the third panel of Figure 7. Strong O VII lines, however, have a large range of O VI EW_s. Part of this spread is due to line saturation and part of it is due to the fact that in warm absorbers the O VI fraction is very low. As pointed out by Chen et al. (2003) who performed the same correlation analysis, this fact suggests that, at least for the stronger lines, follow-up X-ray observations of known O VI absorbers are a promising way to find O VII absorption lines while the opposite strategy is less efficient. Similar considerations apply to O VII and O VIII lines. The scatter in the relation, however, is smaller than in the previous case since these ions have large fractional abundance over a large range of temperatures, a fact that is clearly illustrated in the phase-space diagram of Figure 6. Finally, there is little or no correlation between O VI and O VIII except for strong lines.

In this case, the large scatter reflects the fact that, for a fixed gas density, the temperature of these two species can span a 3 order of magnitudes range. As a result, O VI lines are not able to efficiently flag the presence of O VIII absorbers and vice versa.

4. DETECTING THE WHIM THROUGH ABSORPTION

In this section, we explore the possibility of detecting WHIM in the absorption spectra of X-ray bright objects. We will focus on GRBs, showing that these transient sources offer several advantages over bright AGNs such as quasars and blazars. Then we use our WHIM models to estimate the number of detections that one may expect from a *XENIA/EDGE*-like satellite mission.

4.1. GRBs as Background Sources

Unambiguous WHIM detections require X-ray background sources that are bright, distant, and common enough to provide a good statistical sample of WHIM lines. The latter requirement excludes rare objects, like the Blazars during their active phase. Bright AGNs are quite common but nearby, hence probing relatively short lines of sight. Cross-correlating the VERONCAT catalog of quasars and AGNs (Véron-Cetty & Véron 2006) with the *ROSAT* All-Sky Survey Bright Catalogs (1RXS; Voges et al. 1999), Conciatore (2008) found only 16 objects (mostly BLLac) at $z > 0.3$ with a 200 ks integrated flux (fluence) in the (0.3–2) keV range above 10^{-6} erg cm^{-2}, bright enough to detect WHIM lines. The mean redshift of these objects is ~ 0.5, to be compared with the redshift distribution of the warm hot gas (see, e.g., Figure 1 of Cen & Ostriker 2006) that, at $z \simeq 2$ still accounts for $\sim 20\%$ of the baryonic mass in the universe. GRBs look more promising in all respects. First of all their X-ray afterglows provide a fluence in the (0.3–2) keV similar to that of bright AGNs, collected however in only 50 ks rather than 200 ks. The only disadvantage is represented by their transient nature and by the fact that, since they emit a considerable fraction of the soft X-ray photons soon after the prompt, they require an instrument capable of fast repointing.

In this work, we will focus on GRBs as background sources since the WFM proposed for the *EDGE/XENIA* missions is especially designed to trigger on and localize GRBs and X-ray flashes (XRF) and the satellite can repoint the source in 60 s. Spectra would be taken by the WFS in the 0.2–2.2 keV band by integrating the X-ray flux between 60 s and 50 ks. To convert counts to fluxes, or fluxes from one band to another, and to correct for absorption in our Galaxy and in the host galaxy we assume a typical power-law GRB spectrum with photon index $\Gamma = 2$, absorbed by $N_H(\text{Galaxy}) = 2 \times 10^{20}$ cm^{-2} and by $N_H(\text{Source}) = 3.2 \times 10^{21}$ cm^{-2}.

Given that *EDGE/XENIA* is expected to have orbit and slewing capabilities similar to those of *Swift*, a reliable way to estimate the expected afterglow fluence distribution in a given energy band is to use the total number of photons actually detected for each GRB by *Swift*/XRT in that energy band and converting counts to physical units by adopting the best-fit spectral model of each GRB. In this way, all the effects that may affect the fluence measured by the X-ray telescope (e.g., different times to go on target, Earth occultation statistics and South Atlantic Anomaly (SAA) passage for a satellite in low earth orbit, combined with the different shape and duration of both X-ray prompt and afterglow emissions, X-ray flares, long duration prompt emission, possibility of triggering on a precursor, and thus being on target during the main phase of prompt emission, etc.) are automatically taken into account.

Table 3
GRBs and WHIM Line Detection

$F_{0.5}$	$F_{0.3-10}$	$\#_{GRBs}$	$EW_{O\,VII}$	$\#_{O\,VII}$	$EW_{O\,VIII}$	$\#_{O\,VII+O\,VIII}$
8.8×10^{-7}	2×10^{-6}	33	0.28	58	0.19	37
2.2×10^{-6}	5×10^{-6}	13	0.18	47	0.12	29
4.3×10^{-6}	1×10^{-5}	6	0.12	32	0.08	19

Notes. Column 1: fluence at 0.5 keV (erg cm^{-2} keV^{-1}); Column 2: (0.3–10) keV unabsorbed fluence (erg cm^{-2}) collected during the GRB follow-up observations; Column 3: number of GRBs per year above fluence in an FOV of 2.5 sr; Column 4: minimum EW (in eV) for a 4.5σ O VII line detection in the $B2$ model; Column 5: number of 4.5σ O VII line detections per year in the $B2$ model; Column 6: minimum EW (in eV) for a 3σ O VIII line detection in the $B2$ model; Column 7: number of simultaneous O VII and O VIII line detections per year with significance $\geqslant 5\sigma$ in the $B2$ model.

In the light of these considerations, we have considered, for a sample of 187 GRBs, the total number of counts measured directly by *Swift*/XRT in the (0.3–1) keV band during follow-up observations. We stress that the fluence in the narrow (0.3–1) keV energy band allows to trace well the monochromatic 0.5 keV fluence, which is more relevant to assess the possibility of detecting WHIM lines. In fact, the errors caused by the possible scatter of the GRB population around the typical spectrum, which is used to convert the observed counts in a 0.5 keV fluence (see Column 1 in Table 3), are minimized by using the narrower (0.3–1) keV energy band.

Based on this approach, we estimated that the afterglows with (0.3–1) keV total counts corresponding to a monochromatic fluence 0.5 keV higher than 8.8, 22, and 43×10^{-7} erg cm^{-2} keV^{-1} are, respectively, 9%, 3%, and 1% of the total. These fluence thresholds are listed for reference in the first column of Table 3. In the second column, we also list the corresponding value of the (0.3–10) keV unabsorbed (i.e., corrected for the absorption of the Galactic and the intrinsic hydrogen-equivalent column density) fluence, derived from the (0.3–1) keV counts by assuming the typical GRB afterglow spectrum specified above. Taking into account the *Swift* detection rate of ~100 GRBs per year and the larger solid angle of the WFM on board of *EDGE/XENIA* with respect to the *Swift/*BAT monitor (a factor of ~2 for bursts with prompt fluence of about 1×10^{-6} erg cm^{-2}, and an additional factor of ~3 for larger values of the fluence, see Piro et al. 2009 for details), one expects to observe about 18, 8, and 3 such events per year, respectively.

These numbers represent a conservative estimate based on current *Swift* capabilities. They can be increased in two ways. First of all, reducing the slewing time from the average 120 s required by *Swift* to 60 s would increase the count fluence by a factor of ~2. The amplitude of this effect is quantified by the change in the distribution of the unabsorbed fluence in the (0.3–10) keV shown in Figure 8, where different observation start times from the burst onset are assumed. These fluences have been derived from a sample of 125 *Swift*/XRT light curves, assuming uninterrupted observations (the observed flux in *Swift*, due to the low earth orbit, is basically half of that of an uninterrupted observation), and converting counts to physical units by adopting the best fit spectral model of each GRB. The blue histogram shows the case of a start time from the burst onset of 120 s, equal to the average *Swift* case. Using a satellite like *EDGE/XENIA*, for which the slewing time could be reduced to 60 s, would shift the distribution toward significantly larger values of the fluence, as shown by the red histogram. In that histogram there are three events exceeding 10^{-4} erg cm^{-2}. Two
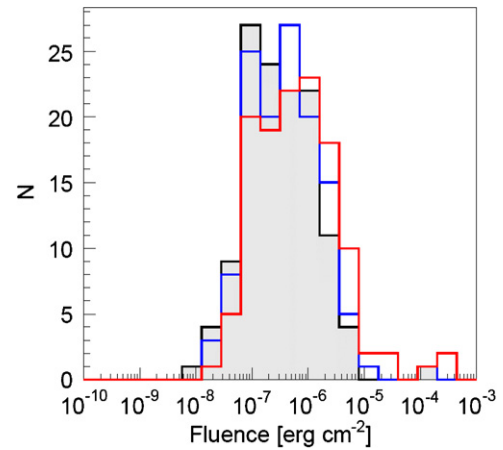

Figure 8. X-ray (0.3–10) keV fluence distribution for 125 GRBs observed by *Swift* with observation start time <1000 s. The three histograms assume different start times and uninterrupted integration intervals. Red curve: 60 s to 60 ks. Blue curve: 120 s to 60 ks. Black curve limiting the shaded area: 180 s to 60 ks.
(A color version of this figure is available in the online journal.)

of them are due to extrapolation of the initial very steep decay. The third one is a really bright but very peculiar event (GRB 060218) with a very long (greater than 35 minutes) prompt emission which was seen by *Swift*/XRT too.

The second improvement is represented by the possibility of detecting and following up of the softest GRB, i.e., the X-ray-rich (XRR) GRBs and the XRFs whose existence have been revealed by *BeppoSAX* (Heise et al. 2001). Their abundance turned out to be comparable to that of classical GRBs. In addition, the observations by *BeppoSAX* (Dálessio et al. 2006) recently complemented by *Swift*/XRT (Gendre et al. 2007) showed that, despite a less energetic prompt gamma-ray emission, the X-ray afterglow flux of XRFs and XRRs is similar to that of GRBs. As a consequence, detecting these populations of objects would significantly increase (almost by a factor of 2) the number of bright afterglows that can be used to study the WHIM. Indeed XRFs constitute about 30% of the *HETE-2* sample, while the combined XRF+XRR sample amounts to 70% of the total (Sakamoto et al. 2005). For reference, XRFs constitute only about 10% of the *Swift* sample (Gendre et al. 2007). This difference is due to the higher lower energy threshold (15 keV) of the BAT trigger instrument, compared to *HETE-2* WXM (2 keV) or to *BeppoSAX* WFC. Adopting a low energy threshold of 8–10 keV, which represents the baseline for the monitor planned for *EDGE/XENIA*, is expected to increase by ~30% the number of detections. With a low energy threshold of 5 keV the increase would be of ~70%.

The cumulative distribution of GRBs that *EDGE/XENIA* is expected to observe in one year as a function of the counts measured in the (0.3–1) keV band is shown in Figure 9 (see the *EDGE* science goal document available at http://projects.iasf-roma.inaf.it/ for further details). Assuming a typical GRB spectrum, we draw three vertical lines at the same reference 0.5 keV monochromatic fluences of 8.8, 22, and 43×10^{-7} erg cm^{-2} keV^{-1} considered above, that correspond to the (0.3–10) keV unabsorbed fluence values listed in Column 2 of Table 3. The number of expected detections above these reference fluence values is 48, 18, and 8, respectively.

In Column 3 of Table 3, we report the number of GRBs that *EDGE/XENIA* is expected to detect above a given fluence threshold, computed by averaging between the pessimistic case, obtained by simply scaling the *Swift* results, and the optimistic case, which accounts for the optimization in the
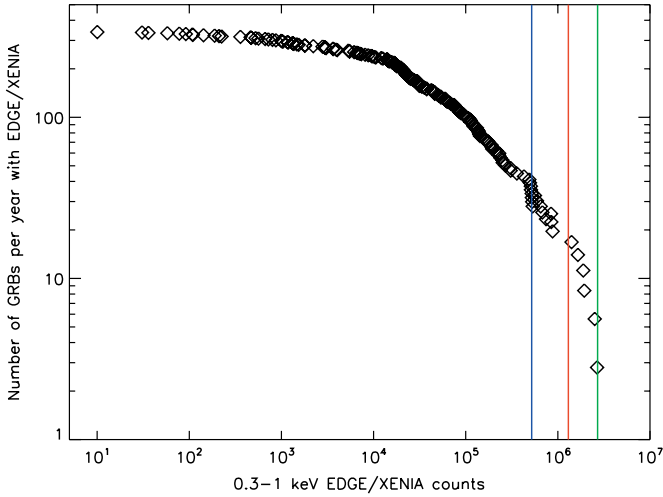
Figure 9. Cumulative distribution of the GRB X-ray afterglows detected per year by a satellite like *EDGE/XENIA* as a function the unabsorbed fluence in the (0.3–1) keV band. The vertical lines are drawn at the three different fluence thresholds of 2, 5, and 10×10^{-6} erg cm^{-2} in the (0.3–10) keV band. These have been obtained assuming the typical GRB afterglow spectrum and column density described in the text.

(A color version of this figure is available in the online journal.)

slewing capabilities and the possibility of detecting XRFs and XRRs in addition to classical GRBs.

As it can be seen, *EDGE/XENIA* is expected to detect in 3 years ~100 GRBs above the fluence threshold indicated in Table 3 compared to the 16 distant AGNs potentially useful for WHIM detection, if observed for 200 ks each. In fact, as we have stressed already, the situation is even more favorable for the WHIM detection since the average redshift of GRBs is significantly larger that AGNs and the probability of line detections is expected to increase accordingly.

4.2. Probability of O VII Detection

In this section, we quantify the detectability of WHIM absorbers by applying the treatment and formalism of Sarazin (1989) to transient sources. We first focus on the problem of detecting the O VII line, which, as stressed before, is usually the strongest absorption feature for the warm hot intergalactic gas.

In Figure 10, we show one realistic mock absorption spectrum of a GRB X-ray afterglow convolved with the *EDGE/XENIA* WFS response matrix. Two WHIM absorbers at two different redshifts (indicated in the plot) are present. In both cases the O VII absorption line stands out prominently along with the O VIII line. The nearest absorber at $z = 0.069$ also shows a weak C VI line. The absorber at $z = 0.298$ instead, is characterized by considerably stronger absorption features including the Fe XVII, Ne IX, and the O VII $1s$–$3p$ lines.

In order to detect an absorption line with statistical significance σ, the detector must collect, within the instrument energy resolution, ΔE, a number of continuum photons $N_{\text{photons}} \gtrsim \left(\frac{S}{N}\right)^2 \left(\frac{EW}{\Delta E}\right)^{-2}$. The corresponding minimum equivalent width EW_{min} for a given line fluence F is

$$\left(\frac{EW_{\text{min}}}{100 \text{ km s}^{-1}}\right) \gtrsim \left(\frac{F}{1.3 \times 10^{-7} \text{ erg cm}^{-2} \text{ keV}^{-1}}\right)^{-0.5}$$

$$\times \left(\frac{E}{1 \text{ keV}}\right)^{-0.5} \left(\frac{\sigma}{3}\right) \left(\frac{\Delta E}{10 \text{ eV}}\right)^{0.5} \left(\frac{A}{10{,}000 \text{ cm}^2}\right)^{-0.5}, \quad (4)$$
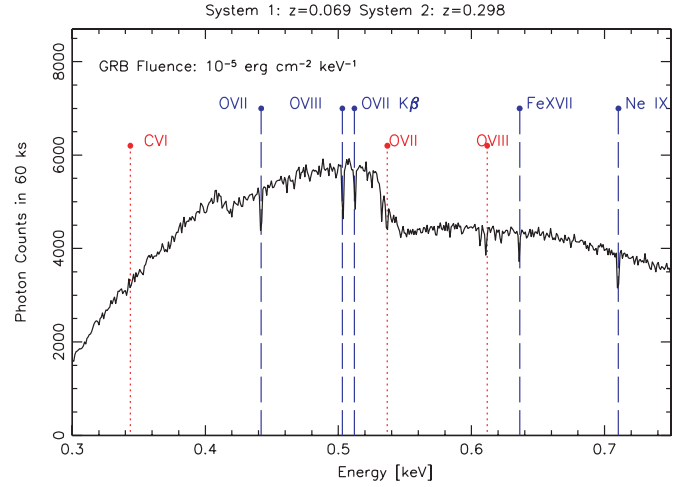
where A is the effective collecting area.

Figure 10. Mock X-ray absorption spectrum of a typical GRB afterglow at $z = 2.6$ convolved with the *EDGE/XENIA* response matrix. The dotted vertical lines mark the most prominent absorption lines produced by a WHIM filament at $z = 0.069$. A second absorption system is also present along the LOS at $z = 0.298$. Its absorption lines are flagged with the vertical dashed lines. The ions responsible for the absorption features are indicated in correspondence of each line. The fluence at 0.5 keV of the afterglow is also shown.

(A color version of this figure is available in the online journal.)

In Column 4 of Table 3, we list the minimum equivalent width required to detect the O VII line with a significance of 4.5σ assuming an energy resolution $\Delta E = 3$ eV and a collecting area $A = 1000$ cm^2 (i.e., matching the baseline configuration of the WFS of *EDGE/XENIA*) in the X-ray spectra of a GRB with a 0.5 keV fluence indicated in Column 2 of the same table. These estimates have been obtained by setting $E = 0.574/(1 + 0.32) = 0.435$ keV in Equation (4), i.e., by assuming that all absorbers are at $z = 0.32$ which is the average redshift of mock absorbers with EW > 0.08 eV in the B2 model. The reason for considering 4.5σ significance is that it guarantees that when two lines (typically O VII and O VIII) can be detected, the underlying absorber is detected with 5σ significance, as will become clear in the next section. The corresponding number of O VII line detections with significance $\geqslant 4.5\sigma$ is listed in Column 5. It was obtained by counting the number of O VII absorbers with EW > EW_{min} (in Column 4) in the mock spectra of model B2 along a number of lines-of-sight equal to that of the expected GRBs listed in Column 3. We recall that the average number of O VII lines above EW is shown in the left panel of Figure 4, in which we can appreciate the differences among the various WHIM models' predictions. Using models M or B1 instead of model B2 which we regard as better physically motivated, significantly reduces the number of expected detections. The exact magnitude of the effect depends on the EW of the line and on the GRB fluence. We estimate that, even with the most conservative model, a satellite like *EDGE/XENIA* should be able to detect about 25 O VII lines per year.

We point out that, in all model explored, the number of expected O VII detections listed in Table 3 is biased low since in our mock spectra we have only considered O VII lines at $z < 1$ ($z < 0.5$ in model M) while, as we have already pointed out, significant amount of WHIM gas are expected out to significantly higher redshifts. In addition, all these estimates should be boosted up by ~40% if the energy resolution of the spectrograph could improve to 1 eV, which constitutes the goal for the WFS.

These estimates for a single O VII line detection, however, must be regarded as hypothetical since with no a priori

knowledge of the absorber's redshift there is no efficient way of preventing contamination by spurious absorption features or confusion with absorption lines form other ions. Of the two effects, confusion should be regarded as the minor one given the paucity of expected non-Galactic absorption lines in the energy range relevant for the WHIM. An effective procedure to minimize confusion is suggested by the analysis of our mock spectra. The idea is to identify the strongest absorption feature with the O VII line (which is often the case), look for all other possible ion lines at the same redshift as the O VII line then move to the next strongest line and so on. The second effect, contamination by Poisson noise, should be dominant. However, its importance decreases with the EW of the O VII line. To quantify the amount of contamination we have produced a number of mock GRB spectra consisting in Monte Carlo realizations of power-law spectra with a specified $N_{\rm H}$ absorption, convolved with the *EDGE/XENIA* response matrix, all of them with a line fluence $F_{0.5}$ in the range $(0.9–4.3) \times 10^{-6}$ erg cm^{-2} keV^{-1}. These mock spectra have been "observed" to compute the probability of fake detections resulting from Poisson fluctuations as a function of the EW of the spurious line. By searching for O VII lines in the energy range $(0.287–0.574)$ keV, corresponding to a redshift range $z = (0–1)$, we computed the minimum EW required to guarantee a contamination level below 1%. The resulting EW$_{\rm s}$ are the same as those listed in Column 4 of Table 3, i.e., they correspond to the minimum EW$_{\rm s}$ required to guarantee a 4.5σ detection of the O VII line. In other words, a 4.5σ detection of a putative O VII line guarantees that contamination by Poisson noise is below 1%.

This exercise illustrates that the simple search for a single O VII line in the GRB spectra observed by *EDGE/XENIA* would provide 25–80 line detections per year, where the lower bound is obtained by considering the most pessimistic among our WHIM models and the upper bound assumes a goal energy resolution of 1 eV. We stress again that out of this sample, we expect at most 1% to be spurious.

Finally, we note that the smallest minimum EW in Table 3 for a joint O VII and O VIII lines detection, which we investigate in the next section, is 0.08 eV. These values require a control of the systematic effects, in particular of the energy width of instrumental bin and the level of the continuum, at ∼2% or better, corresponding to a systematics of 0.06 eV for 3 eV resolution (∼8% for a goal energy resolution of 1eV).

4.3. Probability of Multiple Line Detections

X-ray spectroscopy allows in principle to characterize the physical state of the WHIM and measure its metal content. Unfortunately, the current energy resolution of the microcalorimeters in the soft X-ray band does not allow to resolve the WHIM lines and estimate the gas temperature directly from the line width. Indeed, typical line widths of detectable WHIM absorbers in our mock spectra are in the range 0.1–0.2 eV, well below the goal energy resolution of 1 eV of TES microcalorimeters. Nevertheless, as we shall discuss in the next section, we can still use unresolved lines to constrain the physical state of the absorbing gas, provided that we can detect the absorption line of some other ion in addition to O VII.

To assess the possibility of multiple line detection we first consider the O VIII line that often constitutes the second strongest absorption feature in the mock spectra. Having already identified the redshift of the absorber from the O VII line makes the detection of the O VIII line comparatively easier since one can now be happy with a 3σ rather than a 4.5σ detection.

Table 4
Multiple WHIM Line Detections Involving O VII 1s–2p, O VIII, and a Third Ion

$F_{0.5}$	#$_{\rm O\,VI-x}$	#$_{\rm C\,V}$	#$_{\rm C\,VI}$	#$_{\rm Ne\,IX}$	#$_{\rm Fe\,XVII}$	#$_{\rm Mg\,XI}$
8.8×10^{-7}	4	13	19	23	7	6
2.2×10^{-6}	3	12	18	23	6	5
4.3×10^{-6}	3	7	15	15	6	5

Notes. Column 1: GRB fluence at 0.5 keV (erg cm^{-2} keV^{-1}); Column 2: detections per year involving O VI 1s–2p; Column 3: detections per year involving C V; Column 4: detections per year involving C VI; Column 5: detections per year involving Ne IX; Column 6: detections per year involving Fe XVII; Column 7: detections per year involving Mg XI.

The minimum EW for such detection can be obtained from Equation (4) and is listed in Column 6 of Table 3 as a function of the GRB fluence. Like in the previous case of single O VII line detection, we have only considered O VIII absorption systems with $z \leqslant 1$ and evaluated the minimum equivalent width of the line at $z = 0.32$, i.e., using $E = 0.495$ keV in Equation (4).

We find that ∼50% of all 3σ O VIII lines are associated with a 4.5σ O VII line, i.e., the cumulative distribution function of O VIII and O VII line pairs lies a factor of two below that of the O VIII line alone, plotted in the right panel of Figure 4. The average ratio between EW$_{\rm min}^{\rm O\,VIII}$ and EW$_{\rm min}^{\rm O\,VII}$ is ∼0.7, that is to detect the O VIII line associated with a 4.5σ detected O VII line, the following condition must be satisfied EW$_{\rm O\,VIII} > 0.7$EW$_{\rm O\,VII}$. Moreover, using Monte Carlo simulations we have verified that a joint O VII 4.5 σ and O VIII 3 σ detection corresponds to an overall ∼5σ detection of the underlying absorption system, further reducing the probability of spurious lines contamination.

Since the bulk of the WHIM is not in collisional ionization equilibrium, the EW ratio of two lines depends on both the temperature and the density of the absorbing gas. Therefore, the simultaneous observation of the O VII and O VIII lines alone cannot constrain the physical state of the WHIM. Instead, as we will show in the next section, a third line, preferably of the same element, must be detected as well. To estimate the number of absorbers featuring at least three lines we looked for all mock absorption systems in which an additional 3σ line is detected in association with a 4.5σ O VII line and 3σ O VIII line. Table 4 shows the expected number of such simultaneous detections per year as a function of the GRB fluence. We did not include O VII 1s–3p in the table since its detection would only increase the statistical significance of the absorption system but give no insight on its physical state (the EW ratio of the O VII 1s–3p and O VII 1s–2p lines only depends on their relative oscillator strength).

Detecting three lines of the same elements, such as O VI, O VII, and O VIII, would allow to probe the physics of the WHIM directly. Unfortunately, as shown in Table 4, the X-ray O VI line is very weak and the number of expected multiple oxygen lines detection per year is very small. For this purpose one should use the O VI UV line whose detection in the GRB spectra would require simultaneous UV and X-ray spectroscopy.

Table 4 shows that the best chances to observe multiple line absorption systems would be through the C VI or Ne IX lines. In these cases, however, to assess the physical state of the WHIM, the relative abundance of the elements needs to be specified a priori. Sticking to these ions we have found very few cases of multiple detections, which does not include both the O VII, and the O VIII lines. Also, a significant fraction of multiple line detections consists of more than three lines, i.e., the total number of multiple detections expected per year is less than the sum of all entries in the columns of Table 4.

5. PROBING THE PHYSICAL STATE OF THE WHIM AND ITS COSMOLOGICAL ABUNDANCE

The analysis of X-ray absorption spectra can provide much more than a mere WHIM detection. In this section, we address the problem of determining the temperature and density of the warm hot gas and its cosmological density. To explore the different WHIM models available, all results shown in this section were first obtained for model $B1$ and then checked their validity for model $B2$. Because of the paucity of multiple-line absorption systems, we did not extend the analysis to the mock spectra of model M.

5.1. Measuring the Density and the Temperature of the WHIM

As already mentioned, the quantitative analysis of the absorption spectra is complicated by the fact that the X-ray absorption lines cannot be resolved by currently proposed microcalorimeters. On the other hand, the weak WHIM lines are expected to be optically thin so that a simple linear relation holds between the line equivalent width and the ion column density:

$$\mathrm{EW_P}\ (\mathrm{km\ s^{-1}}) = \frac{\pi e^2}{m_e c}\lambda(X^i)f_{X^i}N_{X^i},\qquad(5)$$

where X^i represents the ion of the element X, $N_{X^i} \equiv \int n_{X^i}(y)dy$ its column density, $\lambda(X^i)$ is the wavelength of the transition, and f_{X^i} is the oscillator strength. From now on we use the subscripts $_\mathrm{P}$ to indicate predicted values and $_\mathrm{M}$ to indicate the values measured from the spectra. In Equation (5), $\mathrm{EW_P}$ is expressed in km s^{-1}, the same units that we will use throughout this section.

Equation (5) allows to estimate the column density of the ion from the EW of the absorption line. However, with no a priori information on the size of the absorbing region, one cannot use the measured EW to estimate the actual density of underlying gas and assess its cosmological density. However, some insights on the physical state of the absorber can be obtained from the EW ratios of at least three different ion lines. In the optically thin limit the EW ratio between any two lines is

$$\frac{\mathrm{EW_P}(X^i)}{\mathrm{EW_P}(Y^j)} = \frac{\lambda(X^i)}{\lambda(Y^j)}\frac{f_{X^i}}{f_{Y^j}}\frac{X^i}{Y^j}\frac{A_X}{A_Y},\qquad(6)$$

where X_i and Y_j represent the two ion fractions while the ratio between A_X and A_Y represents the relative abundance of the element X compared to Y. Equation (6) has been derived from Equation (5) assuming that the density of the ions is constant across the absorber and can be used to infer the density and temperature of the gas upon which the ionization fractions X_i and Y_j depend. Here, we apply Equation (6) to estimate the density and temperature of the absorbing systems in our mock spectra, hence using an approach similar to that of Nicastro et al. (2005) to analyze the physical state of the two putative WHIM absorbers along the LOS to Mrk 421. For this purpose we use the same grids of hybrid collisional ionization plus photoionization models that we have used to draw the mock spectra from the hydrodynamical simulations. These models are used to predict the ratio X^i/Y^j which we substitute in Equation (6) to obtain $\mathrm{EW_P}(X^i)/\mathrm{EW_P}(Y^j)$ as a function of gas density, temperature and ionization background for a given relative metallicity A_X/A_Y, assumed a priori. In a second step, we compare the predicted value of $\mathrm{EW_P}(X^i)/\mathrm{EW_P}(Y^j)$ with that measured from the mock spectra, $\mathrm{EW_M}(X^i)/\mathrm{EW_M}(Y^j)$, to
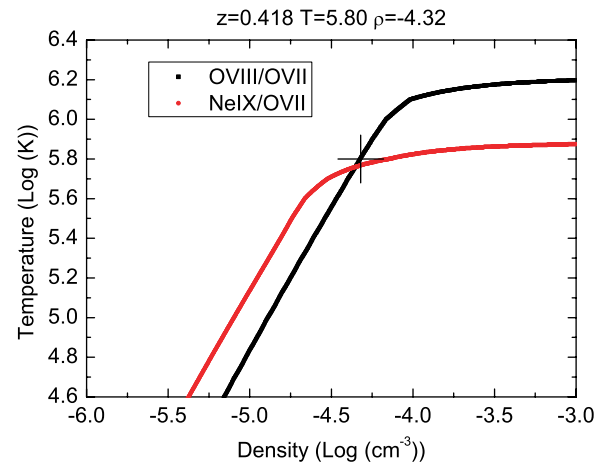

Figure 11. Locii of the minima for the function $\left[\frac{\mathrm{EW_M}(X^i)}{\mathrm{EW_M}(Y^j)} - \frac{\mathrm{EW_P}(X^i)}{\mathrm{EW_P}(Y^j)}\right]^2$ in the (ρ_g, T_g) plane. The two curves refer to a mock absorber at $z = 0.418$ for which we have detected the O VII, O VIII, and Ne IX lines. The cross indicates the expected values.

(A color version of this figure is available in the online journal.)

estimate the density and the temperature of the absorbing gas. Unlike Nicastro et al. (2005) we do not attempt to use this approach in combination with the measured EW of the lines to estimate the metallicity of the gas and constrain the hydrogen column density.

In our analysis, we only considered absorption systems with unsaturated O VI, O VII, O VIII, and Ne IX lines with EW > 20 km s^{-1}, i.e., strong enough to be detected. For the O VI we have also considered weaker lines with EW > 5 km s^{-1} potentially observable in the UV spectra. The density and temperature of the gas can be found by minimizing the difference between $\mathrm{EW_P}(X^i)/\mathrm{EW_P}(Y^j)$ and $\mathrm{EW_M}(X^i)/\mathrm{EW_M}(Y^j)$, and considering at least two independent EW ratios. Figure 11 illustrates the outcome of this minimization procedure. Each curve represents the locus of the minima for the function $\left[\frac{\mathrm{EW_M}(X^i)}{\mathrm{EW_M}(Y^j)} - \frac{\mathrm{EW_P}(X^i)}{\mathrm{EW_P}(Y^j)}(\rho_g, \mathrm{T_g})\right]^2$ in the phase space, given the measured ratio $\mathrm{EW_M}(X^i)/\mathrm{EW_M}(Y^j)$. The two curves refer to the O VIII/O VII and Ne IX/O VII ion ratios. The estimated value for the gas density and temperature is found at the interception between the two curves. The cross indicated the "true" density and temperature of the absorbing gas. As already discussed in Section 3.1 these values of ρ_g and T_g are somewhat ill-defined since the physical state of the gas can vary across the absorbing region and the effective values of its density and temperature depend on ion considered and on the estimator adopted to measure its opacity. This ambiguity can be regarded as an intrinsic uncertainty in the density and temperature of the absorbing gas. In Section 3.1, we have used two different estimators (Equations (2) and (3)) to quantify this uncertainty and found that the typical difference in both temperature and density found when using either estimator is 15%–20% represented by the size of the cross in Figure 11. To further assess the amplitude of this scatter we have used yet another estimator in which the temperature and the density of the gas are measured in correspondence of the minimum of the absorption line. Using the full battery of the three estimators confirms that intrinsic uncertainty in the density and the temperature of the absorbing gas is 15%–20%.

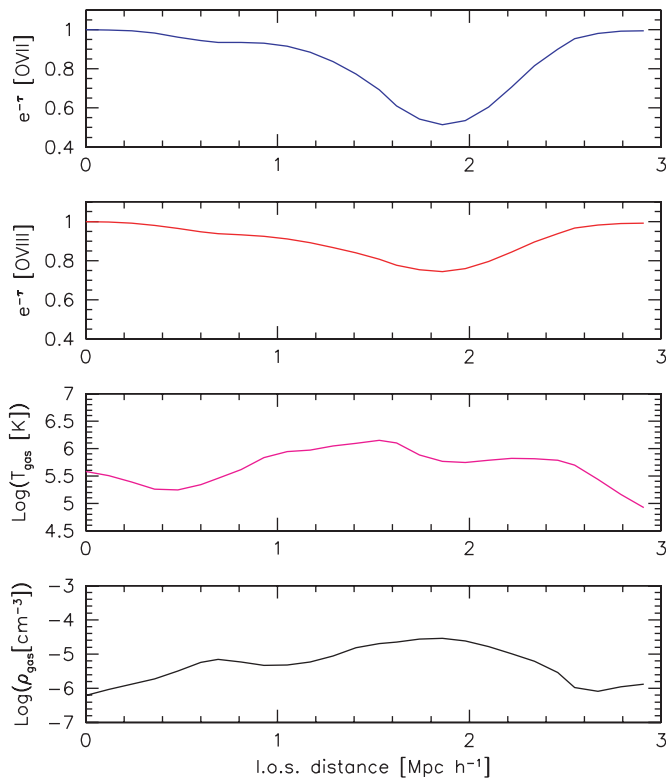The results presented in this section refer to the mock absorbers for which we can measure the O VII/O VIII and Ne IX/

Figure 12. Example of a typical unsaturated WHIM absorber in our mock spectra from model $B1$. From top to bottom: transmitted flux for O VII, O VIII, temperature, and density of the gas along the LOS distance.

(A color version of this figure is available in the online journal.)

O VII EW ratios. Solutions to the minimization procedure are searched for in the phase-space region with $10^{4.5} < T_g < 10^7$ K and $10^{-6} < \rho_g < 10^{-3}$ cm^{-3}, corresponding to overdensities in the range $5 < \delta_g < 5000$, i.e., slightly larger than the canonical WHIM range. In $\sim$70% of the cases, we have been able to estimate the physical state of the absorbers. For the remaining $\sim$30% of the absorbers, we fail to find a common solution, i.e., the two curves do not cross in the explored density–temperature range. We have checked that if we include the third, nonindependent curve relative to EW ratio of Ne IX/O VIII, the resulting additional crossing points are close to the original one.

To assess the accuracy of our procedures in the 70% successful cases, we have compared the ρ_g and T_g estimated through the minimization procedure with the true values. Random and systematic errors can be appreciated from scatter plots such as those in Figures 14 and 15 that refer to the mock absorption systems featuring detectable O VII, O VIII, and Ne IX lines. The estimated gas density turned out to be systematically smaller than the true one by about 35%, similar in size to the random error of $\sim$50% that we identify with the scatter around the best fitting line in the plots. The temperature is overestimated by about 35%, with a random error of the same amplitude. Using O VI instead of Ne IX leads to similar, although somewhat smaller, systematic and random errors.

These errors may originate either from the presence of strong inhomogeneities within the absorbing gas or from the breakdown of the optically thin approximation. To check the validity of the first hypothesis we have examined the behavior of the temperature and the density within the redshift range of the lines corresponding to the WHIM absorbers. Figure 12 is analogous to Figure 2 and shows a typical unsaturated
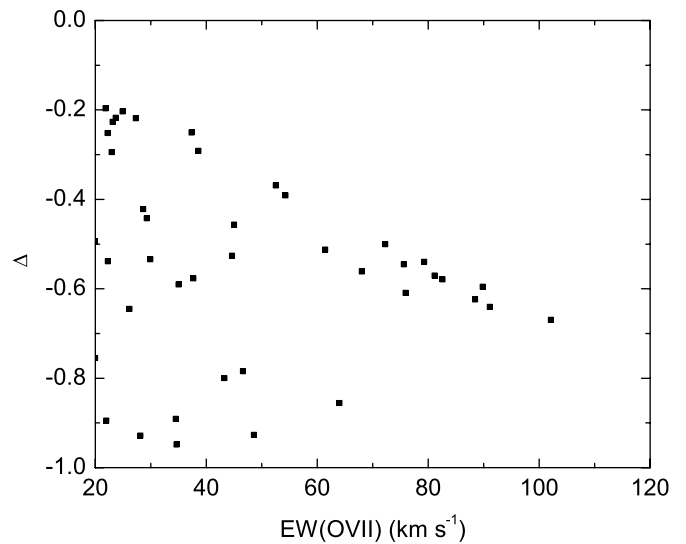

Figure 13. Fractional difference Δ, between $\frac{EW_P(Ne\,IX)}{EW_P(O\,VII)}$ and $\frac{EW_M(Ne\,IX)}{EW_M(O\,VII)}$ as a function of $EW_M(O\,VII)$. Absorbers with unsaturated lines with EW > 20 km s^{-1} are shown with black filled dots.
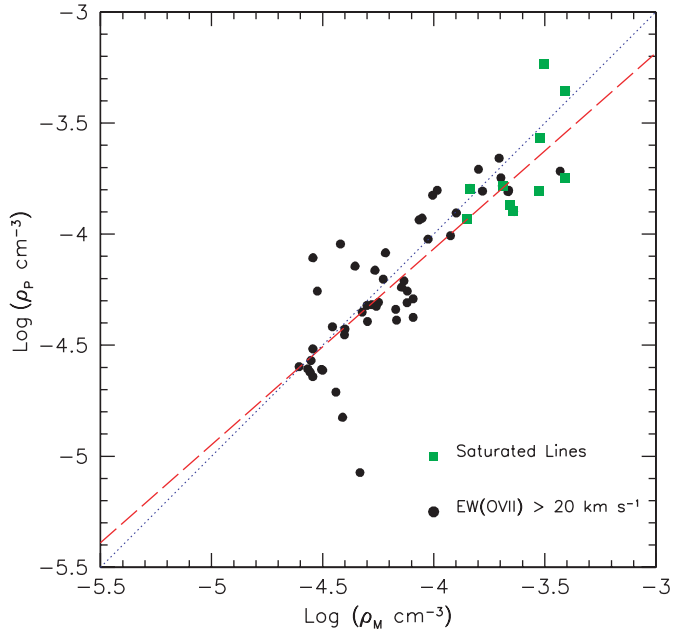

Figure 14. Scatter plot of the predicted gas density, ρ_P vs. measured gas density ρ_M after correction for systematic errors. The filled dots refer to all absorbers with EW(O VII) > 20 km s^{-1} and filled green squares to absorbers which are saturated in any of the lines. The dashed red line represents the best fit to the unsaturated points.

(A color version of this figure is available in the online journal.)

mock absorber. The temperature and the density of the gas are remarkably constant across the redshift range of the O VII and O VIII lines. This result is at variance with that found by Kawahara et al. (2006). The authors found large deviation from homogeneities in the absorbing gas, as clearly illustrated in Figure 15 of their paper. This discrepancy can be understood by noting that Kawahara et al. (2006) absorbers are typically found in regions of higher density and temperature than ours, i.e., within environments in which density and temperature vary change significantly across a $\sim$Mpc scale. Such a difference probably derives from the fact that the O VII ionization fraction and the overall gas metallicity in Kawahara et al. (2006) WHIM model are smaller than in our case.
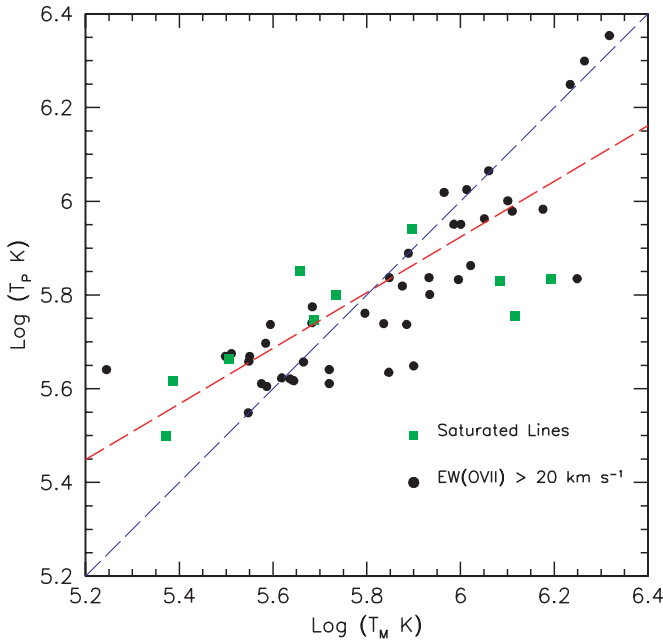
Figure 15. Scatter plot of the predicted gas temperature, T_P vs. measured gas temperature T_M after correction for systematic errors. The filled dots refer to all absorbers with EW(O VII) > 20 km s^{-1} and filled green squares to absorbers which are saturated in any of the lines. The dashed red line represents the best fit to the unsaturated points.

(A color version of this figure is available in the online journal.)

To test whether the systematic errors in the estimate of ρ_g and T_g can be attributed to departures from the optically thin approximation we have computed fractional difference between the measured and the predicted EW ratio computed using the true values of density and temperature, $\Delta = \left[\frac{\mathrm{EW_P(Ne\ IX)EW_M(O\ VII)}}{\mathrm{EW_P(O\ VII)EW_M(Ne\ IX)}} - 1 \right]$. The breakdown of the optically thin approximation leads to overestimate the equivalent width of the line, $\mathrm{EW_P} > \mathrm{EW_M}$. This mismatch is more serious for O VII, which is the strongest line, and should increase with the strength of the line. As a consequence we expect a negative Δ with an amplitude that increases with $\mathrm{EW_M(O\ VII)}$. This effect can indeed be appreciated from Figure 13 in which, superimposed to the scatter, there is a clear trend for Δ to decrease with $\mathrm{EW_M(O\ VII)}$. The scatter is particularly large for weak lines. It is contributed by the fact that the validity of the approximation does not solely depend on the EW of the O VII line and, to a lesser extent, by the presence of inhomogeneities in the absorbing gas. Although we show only the case of Ne IX and O VII, we have checked that the same trend is found for the other ratios that use the O VIII and O VI lines. We note that the ~30% of the absorbers for which the minimization fails to find a (ρ_g, T_g) solution typically have a large Δ.

The existence of an anticorrelation between Δ and $\mathrm{EW_M(O\ VII)}$ suggests a practical, although approximate way to correct for systematic errors since one can use the Δ–$\mathrm{EW_M(O\ VII)}$ relation in reverse to correct the predicted EW ratio knowing the EW of the O VII line.

To first approximation, this correction should not depend on the WHIM model since for a given gas density, temperature, and relative metal abundance, the predicted EW ratio depends only on the ionization model. Therefore, under the hypothesis of hybrid, photoionization plus collisional ionization, and assuming the same UV and X background we expect that the mean Δ–$\mathrm{EW_M(O\ VII)}$ relation should not depend on the WHIM model.

To check this hypothesis we have repeated the same analysis using model $B2$ instead of $B1$ and found that, at least in the range of EW$_s$ we are interested in, the linear fit to the mean Δ–$\mathrm{EW_M(O\ VII)}$ relation is consistent, within the errors, with the one shown in Figure 13.

Figures 14 and 15 compare the logarithm of the density and temperatures predicted from the O VII, O VIII, and Ne IX EW line ratios to their true values after applying the statistical correction described above. The correction is very effective in reducing systematic but also random errors. Systematic errors on the density and the temperature decrease to ~17% and ~10%, respectively, and are comparable, to random errors of ~23% and ~25%. Similar results were obtained for absorbers featuring the O VI rather than the Ne IX line. In this case, however, systematic errors are further reduced to a few percent level.

To summarize, our analysis shows that one can measure the effective temperature and density of an absorption system by measuring the EW ratio of at least three lines. However, the estimate is affected by systematic errors that are mainly contributed by the breakdown of the optically thin approximation. Nonetheless, once the EW of the O VII line is measured accurately, unbiased estimates can be obtained through simple and robust corrections that depend on the ionization model adopted. Applying this technique to absorption systems featuring the Ne IX line detected in the GRB afterglow spectra measured by *EDGE/XENIA*, one expects to be able to measure the density and temperature of about 16 absorbers per year with ~25% random errors. This estimate is obtained by multiplying the number of detectable absorption systems listed in Table 4 by the 70% success rate of the estimation technique.

We note that this estimate requires a priori knowledge of the Ne/O relative abundance. This need not be true when we focus on those absorbers featuring the O VI, O VII, and O VIII lines. Unfortunately, because of the low O VI column density, the O VI $1s$–$2p$ line is very weak and one expects to detect only ~2 such absorbers per year, as shown in Table 4. Once more, to increase the number of O VI detections one should resort to simultaneous UV spectroscopy.

Finally, we point out that we have only considered neon and oxygen ions. Using all other ions listed in Table 4 would significantly increase the number of absorbers with at least three lines for which one can estimate the temperature and the density of the gas.

5.2. Measuring the WHIM Cosmological Density

Another interesting question is how to estimate the cosmological mass density of the WHIM from the line EW$_s$ measured in the GRB afterglows spectra. As pointed out by Richter et al. (2008) this estimate can be obtained in two steps. First, following the procedure outlined in the previous section, one uses the measured EW$_s$ of the ion lines and their ratios to determine the ion fractions and, from these, the total gas column density for a given metallicity. Then, one integrates the gas column density along LOS to different X-ray sources in order to minimize statistical errors and cosmic variance. Following this procedure, the cosmological density of the WHIM in units of the critical density ρ_c Ω_{WHIM}, can be estimated from all absorption systems featuring the O VII line as

$$\Omega_{\mathrm{WHIM}} = \frac{\mu m_H}{\rho_c} \frac{\sum_{i,j} \left(\frac{A_H}{A_O} \right)_{i,j} \left(\frac{N(\mathrm{O\ VII})}{X(\mathrm{O\ VII})} \right)_{i,j}}{\sum_j d_c(z_j)}, \qquad (7)$$

where $\mu = 1.3$ is the mean molecular weight and m_H is the mass of the hydrogen atom. The index i denotes the absorption systems along the LOS j. Each absorber is characterized by the O VII column density $N_{O\,VII}$, that can be evaluated from the line EW, the ion fraction, $X_{O\,VII}$, which can be evaluated from the EW ratios, and the metallicity (A_O/A_H) that needs to be assumed a priori. The quantity $d_c(z_j)$ denotes the comoving distance corresponding to the redshift range in which absorption systems can be detected along the line of sight j and depends on the assumed cosmology. It is straightforward to generalize Equation (7) to account for all remaining absorption systems with featuring lines different from O VII which, however, are very few.

Nicastro et al. (2005) used an estimator similar to that of Equation (7) to measure Ω_{WHIM} from the putative absorption systems along the LOS to Mrk 421. They assumed that the (A_O/A_H) ratio is constant and that errors are dominated by Poisson noise from low number statistics. Under the same hypotheses, one would expect to estimate Ω_{WHIM} with $\sim 10\%$ accuracy using the $N_{abs} \sim 50$ absorption systems that *EDGE/XENIA* is expected to detect in the GRB afterglows spectra during a three-year observational campaign.

This error estimate is clearly too optimistic since it does not account for the uncertainties in the estimated ion fraction and ignores both the cosmic variance and the fact that different absorbers may have different metallicity. In an attempt to obtain a more realistic error estimate we have measured Ω_{WHIM} using all absorption systems listed in Table 4 through the following, simple estimator:

$$\Omega_{WHIM} = \frac{\langle D_{WHIM} \rangle}{\rho_c} \frac{\sum_{i,j} \rho_{i,j}^g}{\sum_j d_c(z_j)}, \qquad (8)$$

ρ^g represents the effective gas density of the absorber estimated from the EW ratios using the technique described in the previous section and for which we have also estimated the associated errors. $\langle D_{WHIM} \rangle$ represents the average comoving depth of the WHIM absorbers. This quantity has been computed using all mock absorption systems with a detectable O VII line and represents the comoving distance corresponding to the redshift interval $[\underline{z}, \overline{z}]$ in which the transmitted O VII flux is below 95%. Clearly, $\langle D_{WHIM} \rangle$ is expected to depend on the WHIM model adopted. For model $B1$ we found that $\langle D_{WHIM} \rangle = 1.4$ Mpc with a scatter around the mean of 0.6 Mpc that quantifies the random error. Uncertainties on Ω_{WHIM} have been obtained by adding in quadrature the errors in the measured ρ^g and the scatter in D_{WHIM} and by assuming that the total uncertainty decreases as $\sqrt{N_{abs}}$. We neglect the cosmic variance. Under these hypotheses the errors on Ω_{WHIM} is $\sim 15\%$, not too different from the simple Poisson estimate.

Applying Equation (8) to the mock absorption systems we obtain $\Omega_{WHIM} = 0.014 \pm 0.002$, slightly smaller that the expected value $\Omega_{WHIM} = 0.017$. The 1.5σ difference reflects the fact that the distribution of D_{WHIM} is not Gaussian but is skewed toward large values.

This exercise suggests that the analysis of X-ray GRB spectra taken in three years by a satellite like *EDGE/XENIA* should allow to measure Ω_{WHIM} with 15% accuracy. However, we stress that this estimate strongly depends on the WHIM models adopted, which is used either to determine the metallicity of the absorbers, (A_O/A_H), in Equation (7) or their average depth, $\langle D_{WHIM} \rangle$, in Equation (8).

6. DISCUSSION AND CONCLUSIONS

In this work, we have considered different numerical models of the WHIM consistent with currently available observational constraints to assess the possibility of detecting the signature of the missing baryons in the X-ray spectra of distant sources and to study their physical properties. In particular, we focused on the absorption spectra of distant GRB afterglows that could be taken by the WFS on board of the recently proposed *EDGE* and *XENIA* missions. Both satellites are capable of fast repointing, which make them suitable for observing the GRB afterglows during their early, bright phase. We note that although we have only considered absorption spectroscopy the WFS is especially suitable for studying the WHIM in emission, as we will show in a future work. The main results of this study can be summarized as follows.

1. All WHIM models explored provide similar predictions for the cumulative distribution of O VI line EW but not for O VII and O VIII. This fact reflects the differences in the metallicity prescriptions among models, which become more evident in regions of enhanced density and temperature in which the O VII and O VIII ions are more common than O VI. As a consequence the O VI lines are not efficient signposts for the bulk of the WHIM which, instead, is best traced by O VII and O VIII, as already shown by Chen et al. (2003).

2. GRBs are better X-ray background sources than AGN in many aspects. First of all, for a reference fluence in the (0.3–2) keV band of 10^{-6} erg cm^{-2} required to detect the WHIM, the typical GRB distance is larger than that of AGN, hence increasing the probability of WHIM detection. Second of all, GRBs constitute a replenishable reservoir of sources, contrary to AGNs. As a consequence, the total number of GRBs above the reference fluence that *EDGE/XENIA* is expected to detect in a year is already a factor of 2 larger that the total number of available AGNs with $z > 0.3$ with the further advantage that the photons can be collected in half observational time.

3. A satellite like *EDGE/XENIA* is expected to detect 25–60 WHIM absorbers per year along the LOS to ~ 30 GRBs through the O VII line. The statistical significance of the detections is 4.5σ which guarantees that the probability of spurious line contamination is less than 1%. The lower bound corresponds to the most conservative WHIM model considered here (dubbed M) which, however, we regard as less realistic since it assumes a deterministic metallicity–density relation. The upper value derives from a more physically sound WHIM model ($B2$) that accounts for the scatter in the relation. A more realistic upper bound should also account for the possibility of detecting WHIM absorbers beyond $z = 1$, which we have ignored in our analysis. Finally, with a goal energy resolution of 1 eV instead of 3 eV (baseline) the number of expected detections would further increase by about 40%.

4. A significant fraction of the WHIM absorbers detected through the O VII line comes with an additional, detectable O VIII line. The total number of expected WHIM absorption systems featuring both the O VII and O VIII lines is about 35 per year when we consider model $B2$. The simultaneous detection of both lines increases the significance of the detection to 5σ. A large fraction of these systems have a third, detectable ion line, typically of a different element, that further increases the significance of the detection.

5. Measuring the EW of at least three lines allows to characterize the thermal properties of the absorber. Under the condition of hybrid collisional and photoionization equilibrium adopted in our WHIM models and assuming an optically thin medium, we were able to determine the effective density and temperature of the gas in $\sim$70% of the line absorption systems featuring a Ne IX or O VI line in addition to O VII and O VIII. These estimates, however, are affected by systematic errors that derive from the breakdown of the optically thin approximation. A simple, model-independent correction can be applied that allows to remove this systematic effect. As a result one should be able to estimate the logarithm of the temperature and density of about 20 WHIM absorption systems per year with $\sim$25% random errors.

6. Integrating the gas density along the LOS to the multiple line absorbers that a mission like *EDGE/XENIA* is expected to detect during the first three years of the mission, would allow to estimate the cosmological mass density of the WHIM with an accuracy of $\sim$15%. This estimate, however, heavily relies on the assumed gas metallicity which currently constitutes the main uncertainties of the WHIM models.

As soon as they will become available, X-ray observations will be used to validate the WHIM models and therefore to constrain the poorly known metal enrichment mechanisms. Nevertheless, with no rigorous metallicity model available, the abundance of the heavy ions in the WHIM can only be measured by observing the Lyα hydrogen line associated with the X-ray absorbers. The Cosmic Origin Spectrograph will allow to search for broad Lyα absorbers which are likely associated with the WHIM along the LOS to bright AGNs. For transient sources, such as GRBs, a similar study would require the possibility of performing simultaneous X-ray and UV spectroscopy which is currently not envisaged in the *EDGE* or *XENIA* mission concepts. Yet, the success of a combined UV and X-ray spectroscopy strategy strongly depends on how well broad Lyα absorbers trace the WHIM gas. Current data sets provide no clue on their mutual relation. On the theoretical side Chen et al. (2003) found weak correlation between H I and both O VII and O VIII that, as we have stressed already, trace the bulk of the WHIM. However, a dedicated theoretical study must be performed to assess how well a combined UV and X-ray spectroscopy will measure the metal content of the WHIM gas.

Although we did not mention it explicitly, the WFS on board of *EDGE* or *XENIA* offers the possibility of combining emission and absorption analyses. This is an important asset of the *EDGE/XENIA* mission concepts since detecting the O VII resonant line in absorption and the triplet in emission allows to constrain the metal abundance of the WHIM. As in the case of the combined UV and X-ray spectroscopy, the success of this alternative strategy depends on how well WHIM absorbers can trace the emitting gas and on our ability to remove or model the contribution of the different backgrounds/foregrounds. The combined study of the WHIM in absorption and emission is the subject of future work. Here, we anticipate that on average 30% of the line systems detected in absorption can also be seen in emission in deep observations. Figure 16 illustrates one of these cases. The lower panel shows a zoom in a narrow energy interval of the mock spectrum displayed in Figure 10, centered on the O VII and O VIII lines of the absorption system at $z = 0.069$. The upper panel shows the emission spectrum in a 4 arcmin^2 area taken along the same LOS when the GRB is
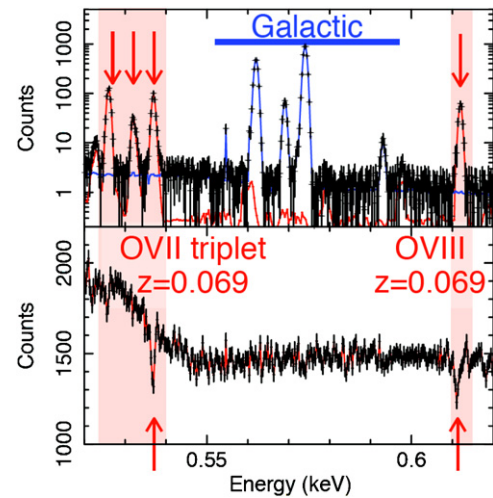

Figure 16. Bottom panel: zoomed plot in a narrower energy range of the mock absorption spectrum in Figure 10, centered on the O VII–O VIII absorption systems at $z = 0.069$. Top panel: emission spectrum in a 4 arcmin^2 area along the same direction, taken in a 1 Ms observation with *EDGE/XENIA* WFS. The O VII triplet and the O VIII resonant line associated with the absorption lines are clearly seen along with the Galactic O VII triplet.

(A color version of this figure is available in the online journal.)

off in a 1 Ms long observation. The O VIII and O VII lines are detected both in absorption and in emission. All components of the O VII triplet are clearly seen and can be well separated from the Galactic component. The combined emission/absorption spectroscopy not only constitutes a possible way to constrain the WHIM metallicity and hence to estimate its cosmological density, but also suggests an observational strategy for the WHIM which consists in preselecting target fields in which the WHIM absorption lines have been detected in the X-ray spectrum of a GRB for deeper, follow-up observations once the GRB has faded away.

The possibility of studying the WHIM in emission is crucial to investigate its spatial distribution, since the pencil-beam-like sampling provided by absorption spectroscopy is too sparse to trace its large-scale, filamentary structure that we observe in the simulations. Yet, cross-correlation of WHIM absorbers and next generation all-sky galaxy surveys out to $z = 2$ like ADEPT or EUCLID may shed light on the WHIM–galaxy connection, very much like in the recent correlation analyses of weak Lyα absorbers and H I-rich galaxies performed by Ryan-Weber (2006) and Pierleoni et al. (2008) and that of O VI absorbers and galaxies (Ganguly et al. 2008). These studies have helped in clarifying the relation between the diffuse baryons in the intergalactic medium and the atoms locked inside virialized structures.

Finally, we would like to stress that although X-ray spectroscopy constitutes the best way to study the missing baryons, alternative strategies like the cross-correlation of the kinetic Sunyaev–Zel'dovich signal near clusters and groups and the all-sky E-mode polarization in the context of upcoming CMB experiments such as *Planck*, ACT, SPT, or APEX will provide useful, independent constraints on the presence and abundance of missing baryons in the universe (Hernandez-Monteagudo & Sunyaev 2008).

REFERENCES

Aguirre, A., Hernquist, L., Schaye, J., Katz, N., Weinberg, D. H., & Gardner, J. 2001, ApJ, 561, 521
Asplund, M., Grevesse, N., & Sauval, A. J. 2005, in ASP Conf. Ser. 336, Cosmic Abundances as Records of Stellar Evolution and Nucleosynthesis in honor of David L. Lambert, ed. T. G. Barnes, III & F. N. Bash (San Francisco, CA: ASP), 25
Boldt, R. 1987, Phys. Rep., 146, 215
Borgani, S., et al. 2004, MNRAS, 348, 1078
Bregman, J. N. 2007, ARA&A, 45, 221
Bryan, G. L., & Voit, G. M. 2001, ApJ, 556, 590
Burles, S., & Tytler, D. 1997, AJ, 114, 1330
Burles, S., & Tytler, D. 1998, ApJ, 499, 699
Cen, R., & Fang, T. 2006, ApJ, 650, 573
Cen, R., & Ostriker, J. P. 1999a, ApJ, 514, 1
Cen, R., & Ostriker, J. P. 1999b, ApJ, 519, L109
Cen, R., & Ostriker, J. P. 2006, ApJ, 650, 56
Chen, X., Weinberg, D. H., Katz, N., & Davé, R. 2003, ApJ, 594, 42
Conciatore, M. L. 2008, Ph.D. thesis, Univ. of Rome "La Sapienza"
Croft, R. A. C., Di Matteo, T., Davé, R., Hernquist, L., Katz, N., Fardal, M. A., & Weinberg, D. H. 2001, ApJ, 557, 67
Dálessio, A., Piro, L., & Rossi, E. M. 2006, A&A, 460, 653
Danforth, C. W., & Shull, J. M. 2005, ApJ, 624, 555
Fabian, A. C., & Barcons, X. 1992, ARA&A, 30, 429
Fang, T., Davis, D. S., Lee, J. C., Marshall, H. L., Bryan, G. L., & Canizares, C. R. 2002, ApJ, 565, 86
Ferland, G. J., Korista, K. T., Verner, D. A., Ferguson, J. W., Kingdon, J. B., & Verner, E. M. 1998, PASP, 110, 761
Fiore, F., Nicastro, F., Savaglio, S., Stella, L., & Vietri, M. 2000, ApJ, 544, L7
Fukugita, M., Hogan, C. J., & Peebles, P. J. E. 1998, ApJ, 503, 518
Fukugita, M., & Peebles, P. J. E. 2004, ApJ, 616, 643
Ganguly, R., Cen, R., Fang, T., & Sembach, K. 2008, ApJ, 678, L89
Gendre, B., Galli, A., & Piro, L. 2007, A&A, 465, L13
Haardt, F., & Madau, P. 1996, ApJ, 461, 20
Heise, J., in't Zand, J., Kippen, R. Marc., & Woods, P. M. 2001, in GRB in the Afterglow Era, ed. E. Costa, F. Frontera, & J. Hjorth (Berlin: Springer), 16
Hellsten, U., Gnedin, N. Y., & Miralda Escudé, J. 1998, ApJ, 509, 56
Hernandez-Monteagudo, C., & Sunyaev, R. A. 2008, A&A, 490, 25
Hickox, R. C., & Markevitch, M. 2007a, ApJ, 661, L117
Hickox, R. C., & Markevitch, M. 2007b, ApJ, 671, 1523
Kaastra, J. S., Werner, N., den Herder, J. W. A., Paerels, F. B. S., de Plaa, J., Rasmussen, A. P., & de Vries, C. P. 2006, ApJ, 652, 189
Katz, N., Weinberg, D. H., & Hernquist, L. 1996, ApJS, 105, 19
Kawahara, H., Yoshikawa, K., Sasaki, S., Suto, Y., Kawai, N., Mitsuda, K., Ohashi, T., & Yamasaki, N. Y. 2006, PASJ, 58, 657
Klypin, A., Hoffman, Y., Kravtsov, A. V., & Gottlöber, S. 2003, ApJ, 596, 19

Komatsu, E., et al. 2009, ApJS, 180, 330
Kouveliotou, C., et al. (the XENIA collaboration) 2008, Proc. AAS 10, HEAD Meeting (Washington, DC: AAS), 37.06
Kravtsov, A. V., Klypin, A., & Hoffman, Y. 2002, ApJ, 571, 563
Mannucci, F., Bonnoli, G., Zappacosta, L., Maiolino, R., & Pedani, M. 2007, A&A, 468, 807
Mathur, S., Weinberg, D. H., & Chen, X. 2003, ApJ, 582, 82
Mazzotta, P., Mazzitelli, G., Colafrancesco, S., & Vittorio, N. 1998, A&AS, 133, 403
Nicastro, F., et al. 2005, ApJ, 629, 700
Paerels, F. B. S., Kaastra, J. S., Ohashi, T., Richter, P., Bykov, A., & Nevalainen, J. 2008, Space Sci. Rev., 133, 405
Pierleoni, M., Branchini, E., & Viel, M. 2008, MNRAS, 388, 282
Piro, L., et al. 2009, Exp. Astron., 23, 67
Rasmussen, A. P., Kahn, S. M., Paerels, F. B. S., den Herder, J. W. A., Kaastra, J. S., & de Vries, C. P. 2007, ApJ, 656, 129
Rauch, M. 1998, ARA&A, 36, 267
Richter, P., Paerels, F. B. S., & Kaastra, J. S. 2008, Space Sci. Rev., 134, 25
Richter, P., Savage, B. D., Sembach, K. R., & Tripp, T. M. 2006, A&A, 445, 827
Roncarelli, M., Moscardini, L., Tozz, P., Borgani, S., Cheng, L. M., Diaferio, A., Dolag, K., & Murante, G. 2006, MNRAS, 368, 74
Ryan-Weber, E. V. 2006, MNRAS, 367, 1251
Sakamoto, T. 2005, ApJ, 629, 311
Sarazin, C. L. 1989, ApJ, 345, 12
Savage, B. D., Sembach, K. R., Tripp, T. M., & Richter, P. 2002, ApJ, 564, 631
Shull, J. M., Roberts, D., Giroux, M. L., Penton, S. V., & Fardal, M. A. 1999, AJ, 118, 1450
Spergel, D. N., et al. 2003, ApJS, 148, 175
Springel, V. 2005, MNRAS, 364, 1105
Springel, V., & Hernquist, L. 2003, MNRAS, 339, 289
Tripp, T. M., Bowen, D. V., Sembach, K. R., Jenkins, E. B., Savage, B. D., & Richter, P. 2006, in ASP Conf. Ser. 348, Astrophysics in the Far Ultraviolet: Five years of Discovery with FUSE, ed. G. Sonneborn, H. Moos, & B.-G. Andersson (San Francisco, CA: ASP), 341
Tripp, T. M., Savage, B. D., & Jenkins, E. B. 2000, ApJ, 534, L1
Tripp, T. M., Sembach, K. R., Bowen, D. V., Savage, B. D., Jenkins, E. B., Lehner, N., & Richter, P. 2008, ApJS, 177, 39
Véron-Cetty, M.-P., & Véron, P. 2006, A&A, 455, 773
Viel, M., Branchini, E., Cen, R., Matarrese, S., Mazzotta, P., & Ostriker, J. P. 2003, MNRAS, 341, 792
Viel, M., Branchini, E., Cen, R., Ostriker, J. P., Matarrese, S., Mazzotta, P., & Tully, B. 2005, MNRAS, 360, 1110
Viel, M., Haehnelt, M. G., & Springel, V. 2004, MNRAS, 354, 684
Voges, W., et al. 1999, A&A, 349, 389
Voit, G. M., & Bryan, G. L. 2001, ApJ, 551, 139L
Weinberg, D. H., Miralda Escudé, J., Hernquist, L., & Katz, N. 1997, ApJ, 490, 564
Yoshikawa, K., & Sasaki, S. 2006, PASJ, 58, 641
Yoshikawa, K., Yamasaki, N. Y., Suto, Y., Ohashi, T., Mitsuda, K., Tawara, Y., & Furuzawa, A. 2003, PASJ, 55, 879
Yoshikawa, K., et al. 2004, PASJ, 56, 939
Zappacosta, L., Maiolino, R., Mannucci, F., Gilli, R., & Schuecker, P. 2005, MNRAS, 357, 929